# SARS-CoV-2 Orf6 is positioned in the nuclear pore complex by Rae1 to inhibit nucleocytoplasmic transport

Tadashi Makio[a], Ke Zhang[b,c], Nicole Love[a], Fred D. Mast[d], Xue Liu[c], Mohamed Elaish[a], Tom Hobman[a], John D. Aitchison[d,e,f], Beatriz M. A. Fontoura[b], and Richard W. Wozniak[a,*]

[a]Department of Cell Biology and Li Ka Shing Institute of Virology, University of Alberta, Edmonton, AB, Canada T6G 2H7; [b]Department of Cell Biology, University of Texas Southwestern Medical Center, Dallas, TX 75235; [c]Shanghai Institute of Immunity and Infection, Chinese Academy of Sciences, Shanghai 200031, China; [d]Center for Global Infectious Disease Research, Seattle Children's Research Institute, Seattle, WA 98101; [e]Department of Pediatrics, and [f]Department of Biochemistry, University of Washington, Seattle, WA 98195

**ABSTRACT** **The Severe Acute Respiratory Syndrome Coronavirus 2 (SARS-CoV-2) accessory protein Orf6 works as an interferon antagonist, in part, by inhibiting the nuclear import activated p-STAT1, an activator of interferon-stimulated genes, and the export of the poly(A) RNA. Insight into the transport regulatory function of Orf6 has come from the observation that Orf6 binds to the nuclear pore complex (NPC) components: Rae1 and Nup98. To gain further insight into the mechanism of Orf6-mediated transport inhibition, we examined the role of Rae1 and Nup98. We show that Rae1 alone is not necessary to support p-STAT1 import or nuclear export of poly(A) RNA. Moreover, the loss of Rae1 suppresses the transport inhibitory activity of Orf6. We propose that the Rae1/Nup98 complex strategically positions Orf6 within the NPC where it alters FG-Nup interactions and their ability to support nuclear transport. In addition, we show that Rae1 is required for normal viral protein production during SARS-CoV-2 infection presumably through its role in supporting Orf6 function.**

**Monitoring Editor**
Anita Corbett
Emory University

Received: Oct 10, 2023
Revised: Mar 7, 2024
Accepted: Mar 15, 2024

## SIGNIFICANCE STATEMENT

- The nuclear pore complex (NPC) is a target of viral proteins, such as SARS-Cov-2 Orf6, that alter nuclear transport to support virus replication. However, it has been unclear how Orf6 impacts NPC function.
- Here the authors show that Orf6 alters nuclear transport through its binding to the NPC proteins Rae1 and Nup98. The Rae1/Nup98 complex positions Orf6 within the NPC channel where it disrupts the interactions between NPC proteins that function to escort transport factors and their cargoes through the NPC.
- Understanding of the impact of Orf6 on NPC structure and transport may reveal strategies for suppressing its effects on the host immune response.

This article was published online ahead of print in MBoC in Press (http://www.molbiolcell.org/cgi/doi/10.1091/mbc.E23-10-0386) on March 20, 2024.

*Address correspondence to: Richard W. Wozniak (rick.wozniak@ualberta.ca).

Abbreviations used: FG, phenylalanine glycine; GlcNAc, N-acetylglucosamine; GLEBS, Gle2-binding sequence; IFM, immunofluorescence microscopy; IFN, interferon; ISG, interferon-stimulated gene; Kap, karyopherin; NPC, nuclear pore complex; NTF, nuclear transport factor; Nup, nucleoporin; SARS-CoV-2, severe acute respiratory syndrome coronavirus 2; shRNA, short-hairpin RNA; VSV, vesicular stomatitis virus; WGA, wheat germ agglutinin.



## INTRODUCTION

Transport of macromolecules between the nucleoplasm and the cytoplasm is controlled by soluble nuclear transport factors (NTFs) that bind cargo and escort them through nuclear pore complexes (NPCs) by transiently interacting with phenylalanine-glycine (FG)-repeat nucleoporins (Nups) that occupy the central channels of NPCs (Hayama *et al*., 2017; Hoogenboom *et al*., 2021). Among a vast number of cellular processes impacted by nuclear transport are those controlling the cellular response to viral infections. For example, interferons (IFNs) are induced and secreted from cells when they sense viral pathogens (Ivashkiv and Donlin, 2014;

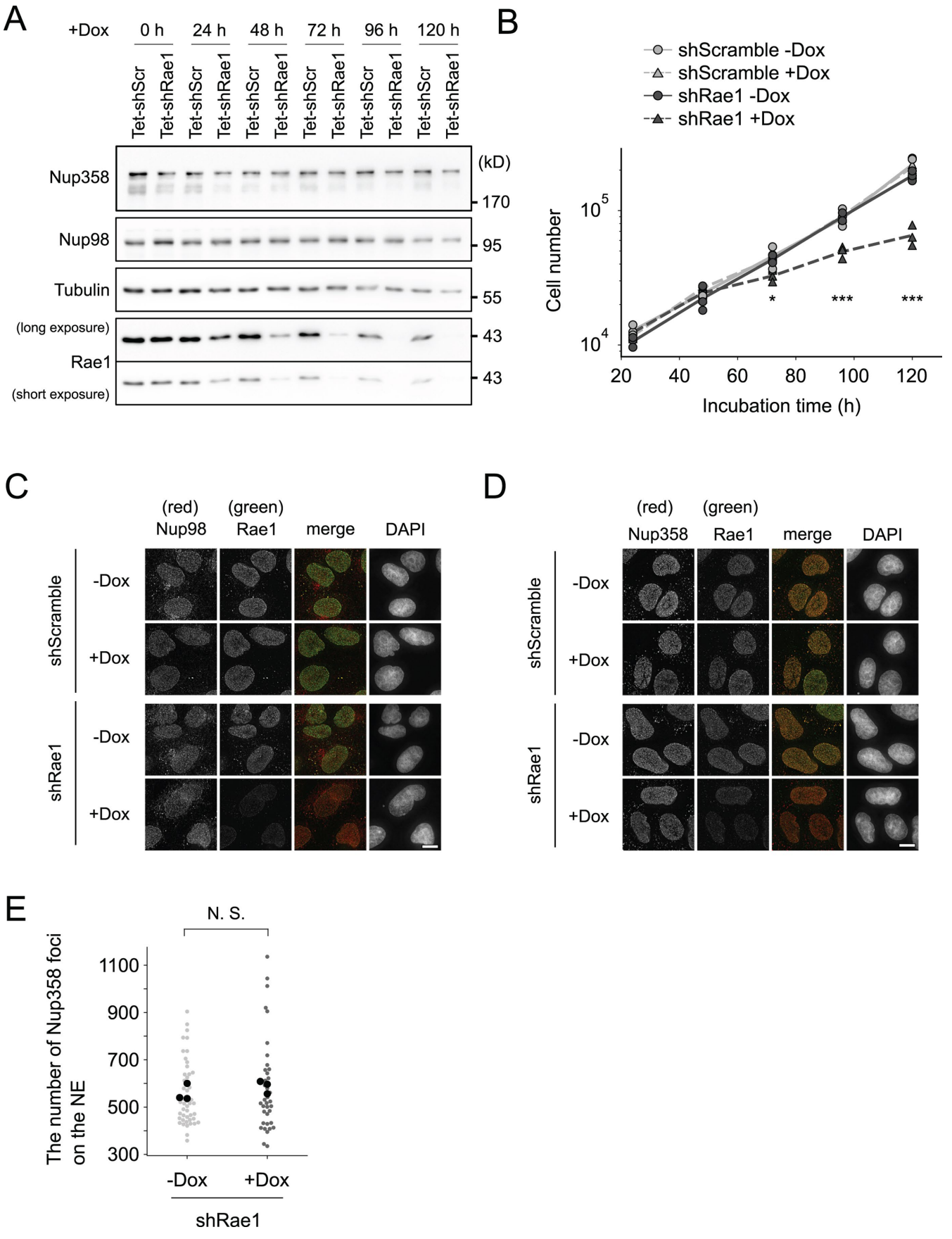
A
+Dox
0 h
24 h
48 h
72 h
96 h
120 h
Tet-shScr
Tet-shRae1
Nup358
Nup98
Tubulin
(long exposure)
Rae1
(short exposure)
(kD)
170
95
55
43
43
B
shScramble -Dox
shScramble +Dox
shRae1 -Dox
shRae1 +Dox
Cell number
Incubation time (h)
C
(red)
Nup98
(green)
Rae1
merge
DAPI
shScramble
shRae1
-Dox
+Dox
D
(red)
Nup358
(green)
Rae1
merge
DAPI
E
N. S.
The number of Nup358 foci on the NE
-Dox
+Dox
shRae1

Hoffmann *et al.*, 2015; Raftery and Stevenson, 2017). Binding of IFN to receptors at the cell surface activates JAK kinases that phosphorylate the transcription activators STAT1 and STAT2 in the cytoplasm inducing their nuclear import by the NTF complex Kap α1(importin α5)/Kap β1 (Sekimoto *et al.*, 1997; McBride *et al.*, 2002). In the nucleus, the STATs activate transcription of interferon-stimulated genes (ISGs) whose products function to suppress various steps in virus production (Schoggins, 2019).

To combat the antiviral activities of the host cells, many viruses have evolved strategies to block IFN signaling, notably employing strategies that selectively alter nuclear transport by targeting the function of NTFs and components of the NPC (Shen *et al.*, 2021). Poliovirus, for example, encodes the 2A protease that cleaves the NPC components Nup62, Nup98, and Nup153 and inhibits protein import pathways and the mRNA export (Gustin and Sarnow, 2001; Castelló *et al.*, 2009). Other examples include the Ebola virus protein VP24 that inhibits nuclear import of activated STAT1 by blocking its binding to the NTF Kap α (Xu *et al.*, 2014), and the Influenza NS1 protein that interacts with the mRNA export factor NXF1 and the splicing machinery to block the export of host mRNA (Satterly *et al.*, 2007; Zhang *et al.*, 2018, 2019).

A conserved target of viruses from several distinct families, including both RNA and DNA viruses, is a complex of two NPC components: Rae1 and the FG-containing Nup98. First identified as a target of the vesicular stomatitis virus (VSV) M protein, binding of the M protein to the Rae1-Nup98 complex interferes with the host transcription and the export of mRNA (von Kobbe *et al.*, 2000; Faria *et al.*, 2005; Rajani *et al.*, 2012; Quan *et al.*, 2014). Two other viral proteins, herpesvirus Orf10 and the severe acute respiratory syndrome coronavirus 2 (SARS-CoV-2) Orf6 protein, also bind to the Rae1-Nup98 complex (Gordon *et al.*, 2020b) and inhibit specific nuclear transport events. Structural analysis of each of these complexes revealed that these viral proteins share a similar binding site on the Rae1-Nup98 dimer (Gao *et al.*, 2022; Li *et al.*, 2022). In cells expressing SARS-CoV-2 Orf6, the nuclear import of the activated, phosphorylated STAT1 (p-STAT1) and the nuclear export of a subset of poly (A) RNAs, including those derived from ISGs, are inhibited (Miorin *et al.*, 2020; Addetia *et al.*, 2021; Hall *et al.*, 2022; Miyamoto *et al.*, 2022). These functions of Orf6 appear to be dependent on its binding to the Rae1-Nup98 complex as a point mutant (M58R) in Orf6 that reduces binding to the Rae1-Nup98 complex (Gao *et al.*, 2022; Li *et al.*, 2022) fails to inhibit the p-STAT1 import (Miorin *et al.*, 2020) or mRNA export (Addetia *et al.*, 2021; Gao *et al.*, 2022). Thus, the apparent IFN antagonist functions of Orf6 (Gordon *et al.*, 2020b) that result from nuclear transport inhibition appear linked to the Rae1-Nup98 complex. However, the mechanism by which Orf6 inhibits transport has been unclear.

We have further examined the physical association of SARS-CoV-2 Orf6 with the Rae1-Nup98 complex and its impact on nuclear transport and NPC structure. For these studies, have constructed the conditional knock down cell lines for depletion of Rae1 and Nup98. While their depletion do not inhibit nuclear import of p-STAT1, it prevented Orf6-mediated import inhibition. Moreover, Orf6 no longer inhibits poly (A) RNA export in cells depleted of Rae1. These and other observations lead us to conclude that the Rae1-Nup98 complex functions to position Orf6 within the NPC where it alters FG-Nup interactions and their association with transport factors, including the Kap α/β1 complex and mRNA export factors.

## RESULT

### Characterization of cell lines depleted of Rae1 and Nup98

To investigate the functional relationship between SARS-CoV-2 Orf6 and Rae1/Nup98 complex, we constructed cell lines containing a RAE1 or NUP98-Nup96 mRNA conditional knockdown cassette consisting of a doxycycline-inducible shRNA construct integrated into the host genome using a lentivirus system (see *Materials and Methods*). We confirmed the conditional depletion of each protein by western blotting. After doxycycline addition, Rae1 was undetectable by 96 h (Figure 1A) while Nup98 and Nup96 levels were strongly reduced by 72 h when compared with the scramble control (Supplemental Figure S1A). Furthermore, both cell lines exhibited somewhat slower growth upon prolonged incubation under depletion conditions (Figures 1B; Supplemental Figure S1B), consistent with the apparent essential functions of *RAE1* and *NUP98* genes (Fontoura *et al.*, 1999; Babu *et al.*, 2003; Walther *et al.*, 2003).

Cells depleted of Rae1 showed no apparent change in NE structure or NPC numbers. Western blotting of cell lysates showed no change in cellular levels Nup98 and Nup358 following Rae1 depletion (Figure 1C). Moreover, immunofluorescence microscopy (IFM)

**FIGURE 1:** Rae1 depletion does not alter Nup or NPC levels. (A) Vero cells harboring a doxycycline-induced shRNA construct (shScramble or shRae1) were incubated in DMEM containing 100 ng/mL doxycycline for the indicated times. Whole cell extracts were prepared, and proteins were analyzed by SDS–PAGE and western blotting using the antibodies directed against the indicated proteins. Two exposures are shown for the anti-Rae1 blot. The positions of molecular mass markers are shown. (B) Vero cells harboring a doxycycline-induced shRNA construct (shScramble or shRae1) were seeded in sixwell plates in the media with or without 100 ng/mL doxycycline. At the indicated time points, the total numbers of cells in the wells were examined ($n = 3$ biological replicates per data point). The Rae1 knock down cells (shRae1) showed a significant reduction in cell proliferation after more than 72 h of incubation with doxycycline when compared with control scramble knock down cells (shScramble) as determined using Student's *t* tests. *: $p < 0.05$, ***: $p < 0.001$. (C and D) Vero cells harboring doxycycline-induced shRNA constructs (shScramble or shRae1) were incubated in DMEM with (+Dox) or without (-Dox)100 ng/mL doxycycline for 120 h and examined by IFM using anti-Nup98 (C) or anti-Nup358 (D) antibodies and anti-Rae1 antibodies. Individual and merged images are shown. These images show the nuclear surface nearest the plate. The position of the nucleus was determined using the DNA stain DAPI. Size bar, 10 μm. (E) The numbers of Nup358 foci on the NE was determined by IFM in the Rae1 knock down cells grown in DMEM with (+Dox) or without (-Dox)100 ng/mL doxycycline for 120 h as shown in panel D. The mean numbers of Nup358 foci per nucleus were calculated for each biological replicate (three biological replicates, $n > 12$ per replicate) and plotted as black filled circles. The individual observations were also plotted as grey dots. A Student's *t* test was carried out to determine whether two population means were equal. N. S., not significant.

of Rae1-depleted cells revealed reduced levels of Rae1, but no apparent visible change in the intensity or number of Nup98 and Nup358 foci at the NE. This conclusion was supported by quantification of the number of Nup358 foci at the NE in WT and Rae1-depleted cells (Figure 1D). To assess classical nuclear localization signal (cNLS)-mediated protein import, we examined the interferon (IFN) induced import of the transcriptional regulator STAT1. IFN treatment induces STAT1 phosphorylation (p-STAT1; Figure 2A) and subsequent nuclear import of p-STAT1 by the karyopherin dimer Kap β1 and Kap α1/importin α5 (Sekimoto *et al.*, 1997; McBride *et al.*, 2002). As shown in Figure 2, B and C, IFN-induced nuclear accumulation of p-STAT1 was unaltered in cells depleted of Rae1. We also examined nuclear export of mRNAs using oligo d(T) probes and fluorescent in situ hybridization. Consistent with previous studies (Babu *et al.*, 2003; Sitterlin, 2004), Rae1 depletion also did not appear to affect poly(A) RNA export as no appreciable nuclear accumulation of oligo d(T) probes was observed in depleted cells when compared with controls (Figure 2D).

Efforts to assess the consequences of Nup98 depletion using shRNA-mediated approaches are complicated by its gene structure, as it is encoded by an mRNA producing a Nup98-Nup96 polyprotein that is cleaved to produce Nup98 and Nup96. Thus, shRNA-mediated depletion leads to reduced cellular levels of both Nup98 and Nup96 detectable by western and IFM analysis (Supplemental Figure S1, A and C). Furthermore, analysis of the number of Nup96 foci at the NE revealed a reduction consistent with a decrease in NPCs (Supplemental Figure S1D). Also, depleted cells show reduced levels of other Nups including Nup358 and Rae1 (Supplemental Figure S1, A, E, and F). Despite of the apparent reduction in NPCs those remaining appeared functional as nuclear import of IFN-induced p-STAT1 levels (Supplemental Figure S2, A–C) appeared unaffected in the Nup98/Nup96-depleted cells. However, nuclear export of poly(A) RNA was inhibited (Supplemental Figure S2D), consistent with previous reports (Powers *et al.*, 1997). Together, these data indicate that Rae1 loss caused no observable changes in NPCs, p-STAT1 import, or export of poly(A) RNA, while NPC numbers and poly(A) RNA export was altered in Nup98/Nup96-depleted cells.

### Orf6 dependent nucleocytoplasmic transport inhibition requires Rae1

Orf6 from SARS-CoV-2, as well as its counterpart from SARS-CoV-1, have previously been shown to inhibit nuclear import, most notably nuclear import of p-STAT1 (Frieman *et al.*, 2007; Miorin *et al.*, 2020; Miyamoto *et al.*, 2022) and nuclear export of poly(A) RNA (Addetia *et al.*, 2021; Hall *et al.*, 2022). Its role in inhibiting p-STAT1 import has been linked to various steps in the transport pathway, including Orf6 binding to p-STAT1, Kap α2 and Kap β1, and Rae1/Nup98 (Frieman *et al.*, 2007; Miorin *et al.*, 2020; Miyamoto *et al.*, 2022), but the specific mechanism remains unclear. To further clarify the role of Orf6 in nuclear protein import inhibition, we examined the consequences of Rae1 and Nup98/Nup96 depletion on the Orf6-mediated import inhibition of p-STAT1. To assess the role of Rae1, the Rae1 depletion cell line, and a scramble control line, were transfected with a *FLAG-ORF6* expression vector (Figure 3). IFM of the scramble lines detected Flag-ORF6 primarily at the nuclear periphery in a punctate pattern that showed extensive overlap with signal observed using antibodies directed against Nup358 (Figure 3A, top two rows), consistent with the previously reported colocalization of Orf6 with Nup98 and Nup358 (Miorin *et al.*, 2020). Strikingly, this localization pattern is dependent on Rae1 as depletion of Rae1 resulted in reduced Orf6 levels at the nuclear periphery, reduced colocalization with Nup358, and increased cytoplasmic Orf6 (Figure 3, A, bottom two rows, and B). Of note, as NE levels of Nup98 were not altered in these cells (Figure 1C), these observations suggest that Orf6 accumulation at NPCs is dependent on Rae1.

Using this same system, we then assessed the function of Rae1 in Orf6-mediated nuclear import inhibition of p-STAT1 (Figure 4). For these experiments, cells were transiently transfected with the Flag-Orf6 expression vector and then treated with vehicle alone or with IFN for 40 min to induce p-STAT1 nuclear import. Cultures transfected with the Flag-Orf6 plasmid showed a mixed population of cells expressing or not expressing Flag-Orf6. In cells expressing Rae1 (shScramble) and lacking detectable levels of Flag-Orf6 (termed bystander cells), nuclear accumulation of p-STAT1 was observed, while those cells expressing Flag-Orf6 failed to accumulate nuclear p-STAT1, consistent with previous observations of (Miorin *et al.*, 2020). In Rae1-depleted cells, Flag-Orf6 expression did not inhibit nuclear accumulation of p-STAT1 and quantification of nuclear:cytoplasmic (N:C) ratios of p-STAT1 revealed a significant increase in the N:C ratio of p-STAT1 relative to control (Figure 4, A and B).

The role of Rae1 in mediating Orf6-dependent poly(A) RNA export inhibition was also examined. In cells producing Rae1, Orf6 production inhibited poly(A) RNA export (Figure 4, C and D). While depletion of Rae1 did not appear to alter poly(A) RNA export (Figures 2D and 4D), inhibition of poly(A) RNA export by Orf6 did require Rae1 (Figure 4D). Together, these data show that, while Rae1 is dispensable for p-STAT1 nuclear import and bulk poly(A) RNA export, it is required to mediate Orf6-dependent inhibition of p-STAT1 import and poly(A) RNA export.

Similar experiments were performed to assess the impact of Nup98/Nup96 depletion on the localization and the function of Orf6. Depletion of Nup98/Nup96 resulted in reduced Orf6 levels at the nuclear periphery, similar to that observed following Rae1 depletion (Supplemental Figure S3). Moreover, as shown in Supplemental Figure S4, Nup98/Nup96 depletion also repressed the inhibitory effect of Orf6 on nuclear import of p-STAT1. These results are likely attributed to, at least in part, the codepletion of Rae1 observed in Nup98/96 depleted cells (Supplemental Figure S2).

### Rae1 supports Orf6-induced change in the Nup98 interacting partners

Orf6 was suggested to alter the localization of Kap α1, Kap α2, and Kap β1 based on data showing that Orf6 inhibits the nuclear accumulation of each of these Kaps (Miorin *et al.*, 2020). We examined the effect of Orf6 on endogenous Kap α2 and Kap β1 localization by IFM. Consistent with previous studies (Lim *et al.*, 2015; Barbato *et al.*, 2020), we detected endogenous Kap α2 and Kap β1 primarily at the NE in a punctate pattern consistent with NPC association. This localization pattern was not altered in cells producing Orf6 and exhibiting p-STAT1 transport inhibition (Supplemental Figure S5). Furthermore, depletion of Rae1, which restored p-STAT1 import in the presence of Orf6, also showed no change in the localization of endogenous Kap α2 and Kap β1.

While Orf6 did not appear to alter levels of Kap α2 and Kap β1 bound to NPC (Supplemental Figure S5), affinity-purification of Nup98 from Orf6-producing cells revealed that the presence of Orf6 led to reduced binding of Kap α1, Kap α2, and Kap β1 to the Rae1/Nup98 complex (Figure 5B and Miorin *et al.*, 2020). Importantly, this reduction in Kaps bound to affinity-purified Nup98 is linked to the transport inhibitory functions of Orf6. Affinity-purification of Nup98 from cells depleted of Rae1 (Figure 5A), which suppressed Orf6-mediated import inhibition (Figure 4), showed that the levels of the

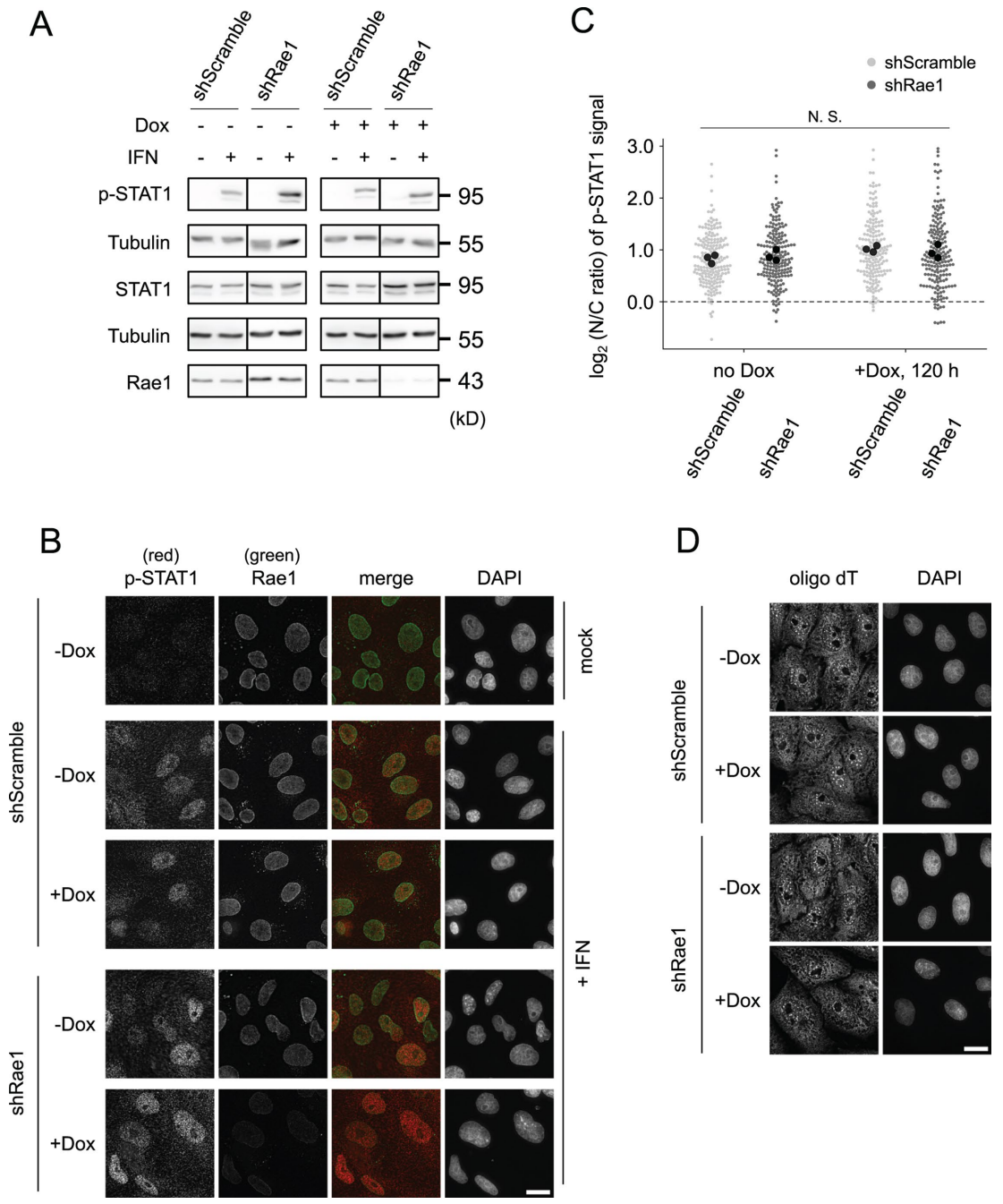


**FIGURE 2:** Rae1 depletion does not alter p-STAT1 import or poly-containing RNA export. (A) Vero cells harboring a doxycycline-induced shRNA construct (shScramble or shRae1) were incubated in DMEM with (+Dox) or without (–Dox) 100 ng/mL doxycycline for 120 h and then treated with IFNα for 40 min. Whole cell extracts were prepared, and proteins were analyzed by SDS–PAGE and western blotting using the antibodies directed against the indicated proteins. The positions of molecular mass markers are shown. (B) Vero cells harboring a doxycycline-induced shRNA construct (shScramble or shRae1) were incubated in DMEM with (+Dox) or without (–Dox) 100 ng/mL doxycycline for 120 h and then treated with IFNα (or mock) for 40 min. The cells were then analyzed by IFM using antiphospho (pY701)-STAT1 (p-STAT1) and anti-Rae1 antibodies. Individual and merged images of p-STAT1 (red) and anti-Rae1 (green) signal are shown. The position of the nucleus was determined using DAPI staining. Size bar, 20 μm. (C) The localization of p-STAT1 shown in panel B was quantified, and the ratio of the signal intensities between the nucleus and the cytoplasm (N/C ratio) were calculated (three biological replicates, $n > 40$ cells per replicate). The mean values of the N/C ratios for each biological replicate were plotted as black filled circles. The individual observations were also plotted as grey dots. The dotted line ($\log_2(N/C) = 0$) denotes the position of equal signal intensities in the nucleus and in the cytoplasm. A one-way ANOVA was carried out to test whether all the mean N/C ratios among the groups are equal. N. S., not significant. (D) Vero cells harboring a doxycycline-induced shRNA construct (shScramble or shRae1) were incubated in DMEM with (+Dox) or without (-Dox) 100 ng/mL doxycycline for 120 h and then examined by FISH using oligo dT probes to detect the localization of poly (A) RNA. The representative microscope images of the poly (A) RNA and the position of the nucleus (DAPI) are shown. Size bar, 20 μm.

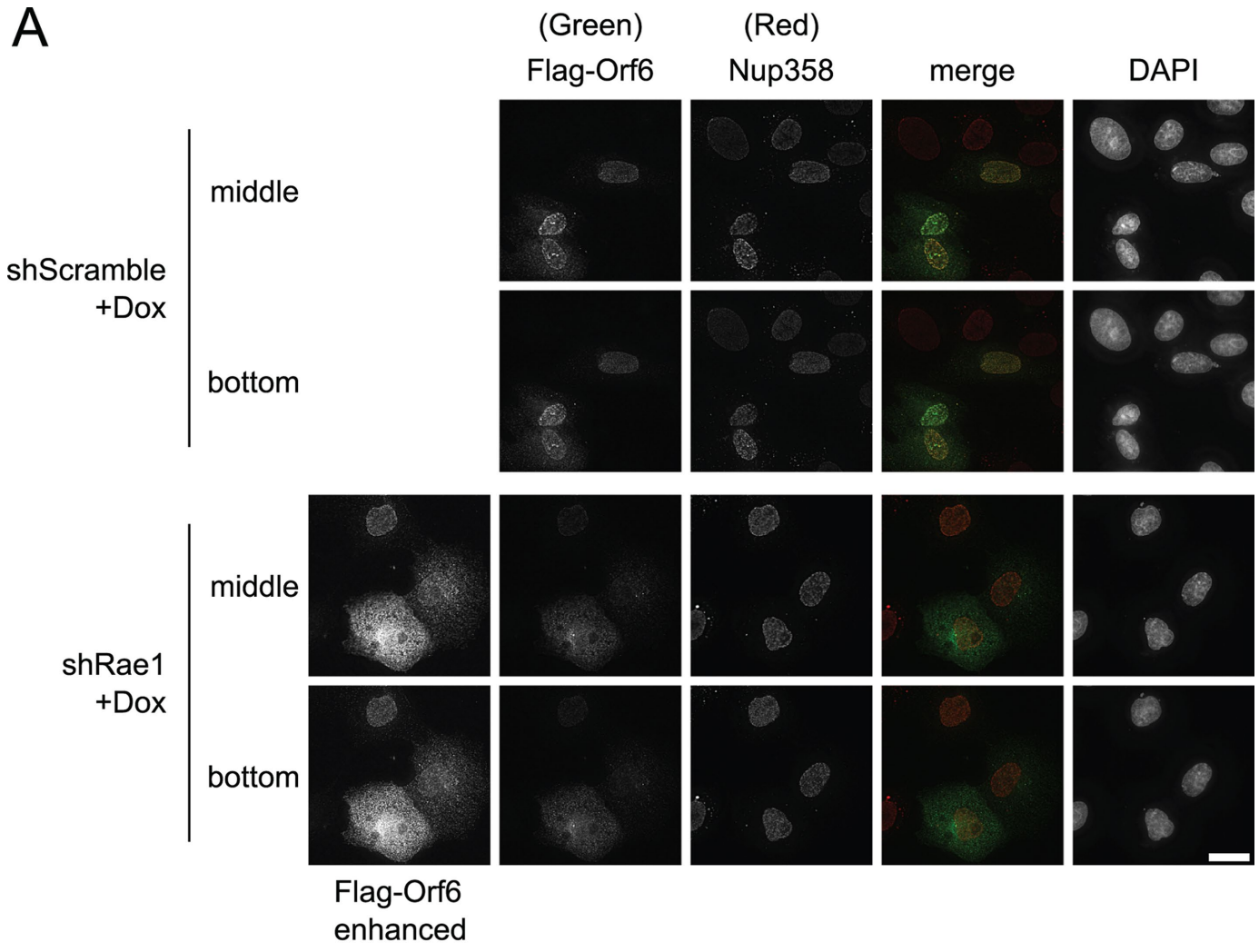
A
(Green)
Flag-Orf6
(Red)
Nup358
merge
DAPI
shScramble
+Dox
middle
bottom
shRae1
+Dox
middle
bottom
Flag-Orf6
enhanced

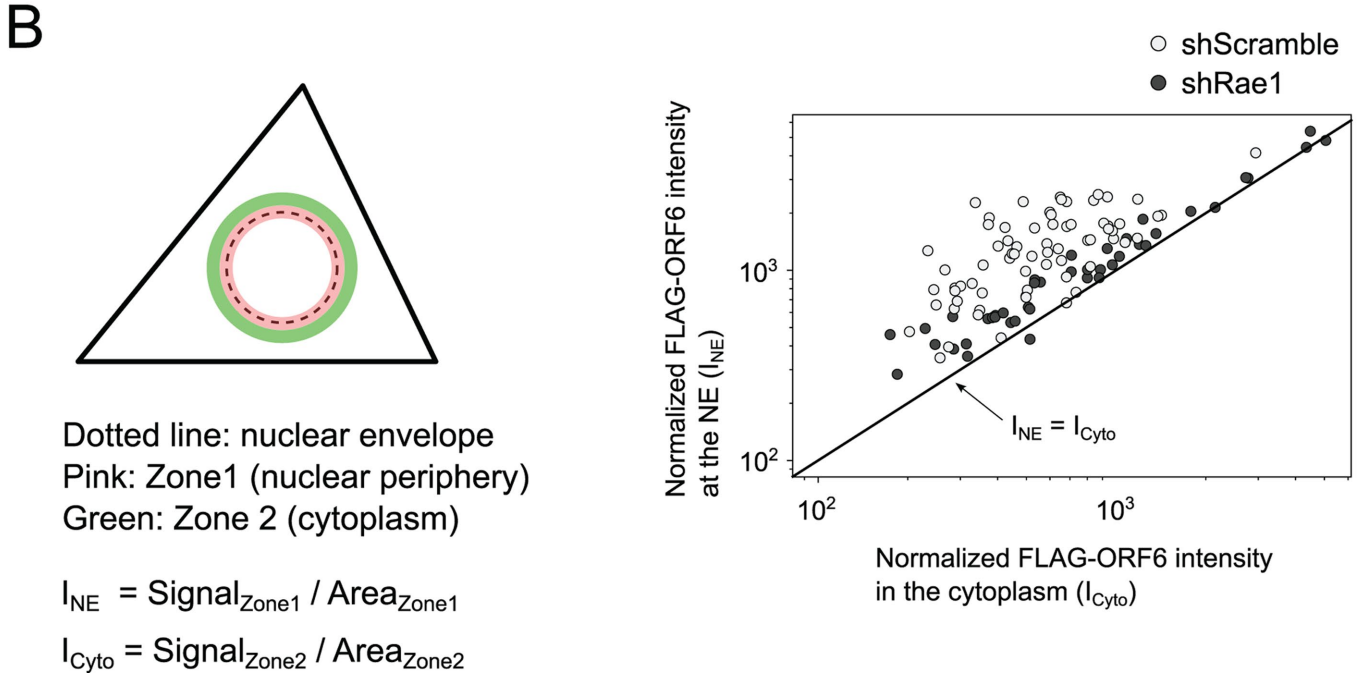
B
Dotted line: nuclear envelope
Pink: Zone1 (nuclear periphery)
Green: Zone 2 (cytoplasm)
$I_{NE}$ = $Signal_{Zone1}$ / $Area_{Zone1}$
$I_{Cyto}$ = $Signal_{Zone2}$ / $Area_{Zone2}$
shScramble
shRae1
Normalized FLAG-ORF6 intensity at the NE ($I_{NE}$)
$10^3$
$10^2$
$I_{NE}$ = $I_{Cyto}$
$10^2$
$10^3$
Normalized FLAG-ORF6 intensity in the cytoplasm ($I_{Cyto}$)

Kap α1, Kap α2, and Kap β1 bound to Nup98 returned to levels similar to (Kap α1 and Kap α2) or higher (Kap β1) than detected in WT cells lacking Orf6 (Figure 5B). These data suggest that Orf6 requires Rae1 to inhibit the association of these karyopherins with Nup98.

The results of our examination of Kap α1, Kap α2, and Kap β1 suggest that Orf6 binding to the NPCs does not alter binding of the bulk of these endogenous Kaps to the NPC, but it reduces their association with purified Nup98 (Supplemental Figure S5, B and D, and Figure 5B). We hypothesized that these latter results may arise due to Orf6-induced changes in the association of Nup98 with neighboring Kap-binding FG-Nups. To test this hypothesis, we probed the affinity-purification Nup98 isolated from cells producing or not producing Orf6 for the presence of interacting FG-Nups. As presented in Figure 6, Nup98 affinity-purified from cells producing Orf6 was associated with lower levels of several FG-Nups, including Nup62, Nup214, and Nup358, relative to control cells. Another FG-Nup examined, Nup153, showed no change. These results suggest that Orf6 alters the interactions of FG-Nups within the NPC. Importantly, the reduced binding of Nup98 to Nup62, Nup214, and Nup358 detected in the presence of Orf6 was suppressed by depletion of Rae1. In cells producing Orf6 and depleted of Rae1 Nup98 binding to these various Nups appeared similar to that observed in WT control cells (Figure 6). These results are consistent with our observation that Rae1 depletion suppresses the transport inhibitory effects of Orf6.

### Rae1 depletion alters viral protein levels in SARS-CoV-2 infected cells

As our data show that Rae1 is a key host factor targeted by SARS-CoV-2 Orf6, we examined the functional consequences of the loss of Rae1 on virus production and viral protein levels. For these experiments, Vero cell derived lines encoding the *RAE1* shRNA conditional knockdown cassette or the shScramble control were treated with doxycycline for 48 h to induce shRNA expression and then infected with SARS-CoV-2 virus. At 24 h post infection (p.i.), viral titers were measured and showed no significant difference between the shSramble and Rae1-depleted cells (Figure 7A). We also examined cellular levels of several viral proteins, including the nonstructural proteins Nsp1 and Nsp8, the two viral structural proteins Spike and Nucleocapsid, and Orf6 in infected Rae1-depleted and control cells. Western blot analysis confirmed Rae1 depletion and little change in the levels of Nsp1 and Nsp8 between Rae1-depleted and control infected cells. Surprisingly, however, Orf6, Spike, and Nucleocapsid were present at higher levels in the infected Rae1-depleted cells when compared with control cells (Figure 7B). Consistent with these observations, IFM analysis showed Nucleocapsid concentrated at viral replication sites (detected with dsRNA antibodies) in control cells, while Rae1-depleted cells contained additional Nucleocapsid often detected throughout the cytoplasm (Figure 7C).

The increased levels of the Spike and Nucleocapsid proteins detected in infected Rae1-depleted cells did not appear to be due to an increase in levels of the subgenomic viral RNA encoding these proteins. As shown in Figure 7D, no change in levels of subgenomic RNAs encoding Spike, Nucleocapsid, and Orf6 were detected between Rae1-depleted and control cells. Thus, increased expression of subgenomic RNA did not accompany the increase in cellular levels of these viral proteins. These observations suggest that Rae1 is also required to suppress steady-state levels of specific proteins encoded by the SARS-CoV-2 genome.

## DISCUSSION

SARS-CoV-2 Orf6 suppresses IFN induction of ISGs. This function of has been linked to its ability to inhibit nuclear transport, including nuclear import of p-STAT1 and export of mRNAs, notably those derived from ISGs (Hall *et al.*, 2022). Previous reports by others and ourselves showing that Orf6 binds to Rae1 and Nup98, as well as the detection of a pool of Orf6 associated with NPCs (Miorin *et al.*, 2020; Addetia *et al.*, 2021; Miyamoto *et al.*, 2022), led to the hypothesis that Orf6 compromises the function of NPCs. How this is accomplished has been unclear. Our data lead us to conclude that Orf6 does not inhibit transport solely by compromising transport functions of Rae1 or Nup98. Rather, our observations lead us to purpose that the Rae1/Nup98 complex functions to position Orf6 within the NPC where it alters FG-Nup interactions and their association with transport factors, including Kap α/ Kap β1 complexes and mRNA export factors.

Structural analysis of the NPC suggests that the Rae1/Nup98 complex is positioned adjacent to the central channel of the NPC (Bley *et al.*, 2022; Mosalaganti *et al.*, 2022). Nup98 contains functional distinct regions including a C-terminal domains that forms linkers between components of the NPC inner ring and segments that extend to the outer ring (Fischer *et al.*, 2015). The N-terminal region of Nup98 contains its FG domains and the GLEBS motif that binds Rae1. This region is predicted to extend into the central channel where Rae1 and the FG-containing region of Nup98 would be positioned in the vicinity of the FG-containing regions of other Nups including Nup62 and Nup214 (Bley *et al.*, 2022; Mosalaganti *et al.*, 2022). Consistent with this positioning, Rae1 and Nup98 have been previously proposed to play a direct role in nuclear transport (Powers *et al.*, 1997; Pritchard *et al.*, 2000; Wu *et al.*, 2001). Here we also detected an inhibition of bulk poly(A) RNA upon depletion of Nup98

**FIGURE 3:** Orf6 association with the NPC is reduced in Rae1-depleted cells. (A) Vero cells containing a doxycycline-induced shRNA construct (shScramble or shRae1) cassette were incubated with 100 ng/mL doxycycline for 120 h and transfected with the plasmid encoding Flag-Orf6 for the last 24 h. The cells were then analyzed by IFM using anti-Flag antibody and anti-Nup358 antibodies. The representative microscope images show the distribution of Flag-Orf6, Nup358, merged images, and the position of nuclei (DAPI). In order assess the colocalization between Flag-Orf6 and Nup358, two difference slices from the stacked images (the bottom [i.e., nearest the plate] and the middle sections of the nuclei) are shown. Size bar, 20 μm. (B) Accumulation of Flag-Orf6 at the NE were quantified. (Left) The schematics of the quantitation strategy. The signal intensities in a region including the NE (Zone 1; nuclear periphery) and a cytoplasmic region just outside of the Zone 1 (Zone 2; cytoplasm) from images such as those shown in (A) were measured. (Right) The scatter plot of the Flag-Orf6 signal intensity at the NE (y-axis) and in the cytoplasm (x-axis) of multiple cells. The diagonal line $I_{NE} = I_{Cyto}$ denotes equal values of Flag-Orf6 signal at the NE and the cytoplasm. Data were obtained from four independent experiments.

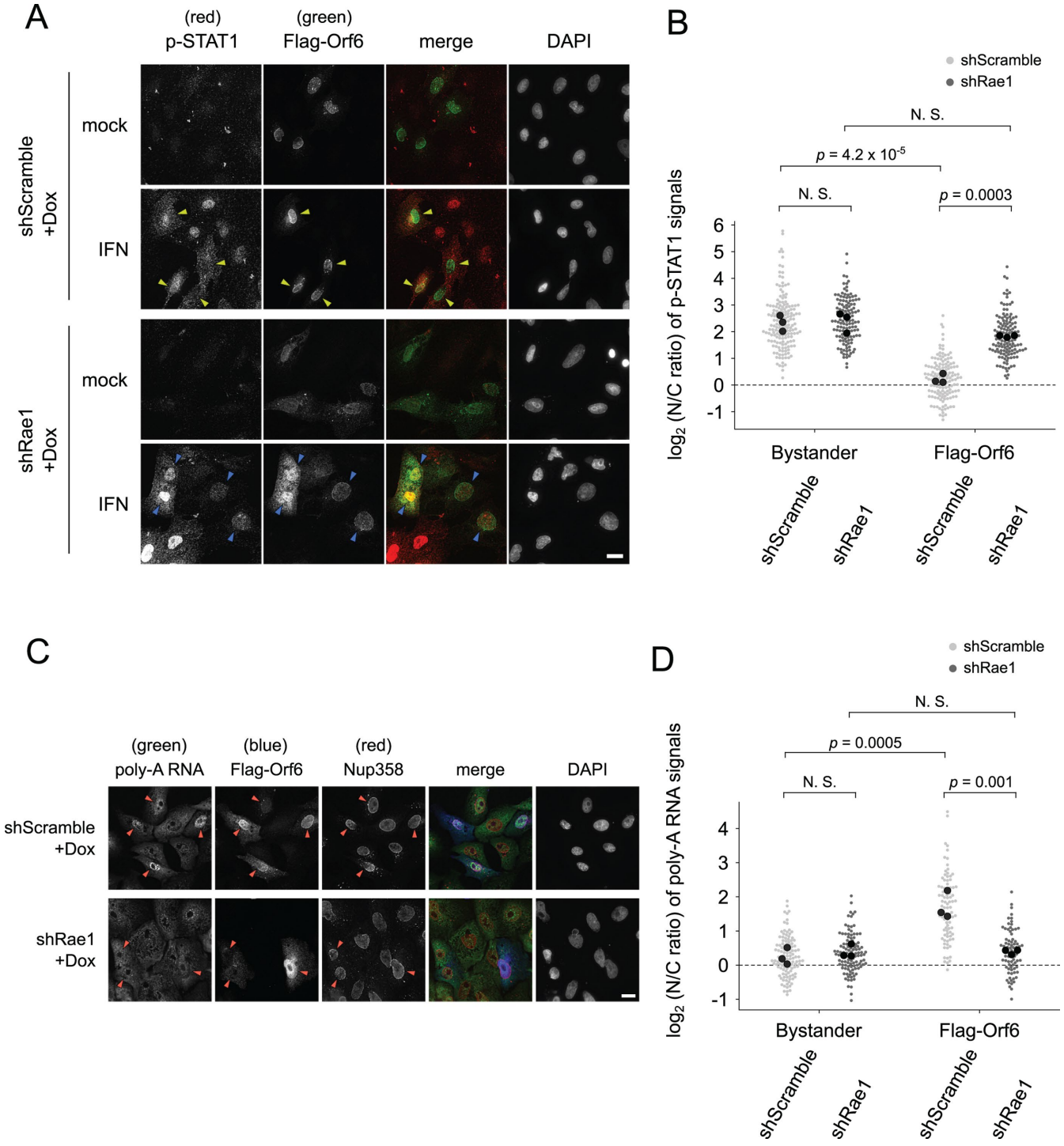


FIGURE 4: Rae1 is required for the nuclear transport inhibitory activity of Orf6. (A) Vero cells containing a doxycycline-induced shRNA construct (shScramble or shRae1) cassette were incubated with 100 ng/mL doxycycline for 120 h and transfected with the plasmid encoding Flag-Orf6 for the last 24 h. Cells were then treated with (IFN) or without (mock) IFNα for 40 min and analyzed by IFM using anti-Flag (Flag-Orf6) and anti-phospho (pY701)-STAT1 (p-STAT1) antibodies. The representative microscope images show the distribution of p-STAT1 and Flag-Orf6, merged images, and the position of nuclei (DAPI). The cells marked by yellow arrowheads indicate the Orf6-positive cells that failed to accumulate the activated p-STAT1 protein in the nucleus after the interferon treatment. The cells marked by blue arrowheads indicate the Orf6-positive cells that accumulated the p-STAT1 protein in the nucleus after the interferon treatment. Size bar, 10 μm. (B) IFN-induced nuclear accumulation of the p-STAT1 was quantified in Rae1-depleted and control cells that were producing or showed no detectable (bystander cells) Flag-Orf6. The ratios between the nuclear and the cytoplasmic signals of p-STAT1 (N/C ratio) were calculated (three biological replicates, $n > 30$ cells per replicate). The mean values of the N/C ratios for each biological replicate were plotted as black filled circles. The individual observations were also plotted as grey dots. The dotted line ($\log_2(N/C) = 0$) denotes the position of equal signal

using situ-hybridization assays (Supplemental Figure S2). By contrast, despite the broader effects on NPCs caused by depleting Nup98, including reductions in cellular level of other Nups (including Rae1) and NPC numbers (Supplemental Figure S2), we detected no obvious defects in IFN-induced nuclear accumulation p-STAT1 in the Nup98-depleted cells. Rae1 depletion, which appeared specific and robust (Figure 1), also caused no detectable defects in either p-STAT1 import, nor did in situ hybridization reveal defects in bulk poly(A) RNA export (Figure 2). This latter observation is consistent with previous results showing cells lacking or depleted of Rae1 do not show bulk poly(A) RNA export inhibition (Babu *et al.*, 2003; Gong *et al.*, 2016). These observations are somewhat surprising as numerous studies have linked mammalian Rae1/Nup98 complex to mRNA transport, including studies showing they bind RNA and the mRNA transport factor TAP/NXF1 (Kraemer and Blobel, 1997; Bachi *et al.*, 2000; Pritchard *et al.*, 2000; Blevins *et al.*, 2003). Our results showing a bulk poly(A) RNA export defect in the Nup98-depleted cells (Supplemental Figure S2D) may reflect a broader role for Nup98 and the Rae1/Nup98 complex. By contrast, Rae1 depletion alone could selectively impact nuclear export of specific mRNA species (Satterly *et al.*, 2007), which may not be detected when examining bulk poly(A) RNA export.

The lack a visible impact of the Rae1 depletion on p-STAT1 import and bulk poly(A) RNA export lead us to conclude that the transport pathways inhibited by Orf6, while likely including those directly mediated by Rae1 (such as a specific subset of mRNAs), also include transport events not directly requiring Rae1, including the transport of p-STAT1 and the bulk of mRNA. Thus, we propose that the role of Rae1 in mediating the transport inhibitory functions of Orf6 is multiple faceted and in large part indirect. We propose that the Rae1/Nup98 complex functions to position Orf6 at a location within the NPC where it can disrupt multiple transport pathways, including mechanistically diverse pathways that regulate protein import and mRNA export. Furthermore, we envisage that this would require the Rae1/Nup98 complex to establish a critical concentration of Orf6 at specific locations within the NPC where it would exert its inhibitory effect. When Rae1 is depleted, we observe that Orf6, while still capable of binding Nup98 (Figure 5B), shows reduced localization to NPCs as detected by IFM (Figure 3A). As Orf6 fails to inhibit transport under these conditions, we concluded that Rae1 functions to support the inhibitory activity of Orf6 by enhancing its binding to, and spatial positioning within the NPC.

Based on structural models of the NPC (Bley *et al.*, 2022; Mosalaganti *et al.*, 2022), we envisage that the Rae1/Nup98 complex positions Orf6 adjacent to the central transport channel and the FG-rich regions of Nups that are predicted to occupy the channel. Here Orf6 could function to alter molecular interactions between FG-nups. Consistent with this idea, we detected Orf6-dependent changes in the interaction partners of Nup98. We show that the association of Nup98 with specific neighboring FG-Nups positioned on the cytoplasmic face of the NPC channel, including Nup62, Nup214, and Nup358 (Bley *et al.*, 2022), but not another FG-Nup Nup153 positioned on the nucleoplasmic face, are reduced in the presence of Orf6 (Figure 6). These results lead us to propose that Orf6-induced changes in the interactions networks between certain FG-nups (including Nup98), alter their binding to NTFs, and inhibit NTF/cargo movement through the NPC central channel. These observations are consistent with data showing that Orf6 reduces the association of Kap α1, Kap α2, and Kap β1 with immunopurified Nup98 (Figure 5; Miorin *et al.*, 2020), an observation that may be explained by a reduction in Kap binding sites (i.e., FG-Nups) in complex with Nup98. Moreover, such a mechanism is also consistent with previous studies showing overexpression of the Kap α1, Kap α2, and Kap β1, while normally exhibiting a steady-state localization to the nucleoplasm, are primarily cytoplasmic in the presence of Orf6 (Miorin *et al.*, 2020; Miyamoto *et al.*, 2022) suggesting their transport through NPCs is inhibited.

Notably, we observed that Orf6 expression did not alter the localization of endogenous Kap α2 and Kap β1, both of which we detect enriched at NPCs in the presence or absence Orf6 (Supplemental Figure S5), nor did it alter the localization of Kap α1 (unpublished data). These results would again suggest that Orf6 does not inhibit binding of NTFs to most FG Nups, but likely blocks their translocation through NPCs. A similar phenomenon was been reported when nuclei are treated with wheat germ agglutinin (WGA), a multivalent lectin that binds to the N-acetyl glucosamine (GlcNAc) moieties present on various FG-Nups (Hanover *et al.*, 1987; Holt *et al.*, 1987). While not affecting NTF-cargo binding to the NPC (Finlay *et al.*, 1987; Newmeyer and Forbes, 1988), WGA, being a multivalent binder of GlcNAc moieties, is thought to alter FG-Nups interactions by potentially creating noncovalent crosslinks between FG-nups that would alter the ability of NTFs to partition through the central channel (Mohr *et al.*, 2009).

We envisage that the diverse transport inhibitory effects of Orf6, including blocking protein import and mRNA export, are caused by alteration in FG-Nup interactions directed by the Rae1/Nup98 complex-mediated positioning of Orf6 within the central channel. However, not all NTFs (and their cargoes) are predicted to be equally affected by these changes as NTFs may follow different pathways through the NPC (Marelli *et al.*, 1998; Wu *et al.*, 2001; Strawn *et al.*, 2004) and, furthermore, some cargoes can be transported by more than one NTF. These diverse pathways through the NPC are likely to give rise to varied changes in cargo transport. For example, Kap α-Kap β1 cargoes such as activated IRF3 and p-STAT1 are

intensities in the nucleus and in the cytoplasm. Multiple comparisons were carried out using a one-way ANOVA followed by pairwise Tukey HSD posthoc tests. N. S., not significant. (C) Vero cells containing a doxycycline-induced shRNA construct (shScramble or shRae1) cassette were incubated with 100 ng/mL doxycycline for 120 h and transfected with the plasmid encoding Flag-Orf6 for the last 24 h. The cell samples were then analyzed by FISH and IFM. The representative microscope images showing the localization of poly (A) RNA, Flag-Orf6, Nup358, the merged images, and nuclei (DAPI). The cells marked by red arrowheads indicate the Orf6-positive cells. Size bar, 20 μm. (D) From the images such as those shown in panel C, the nuclear accumulation of poly (A) RNA in the cells expressing Flag-Orf6 and in the bystander cells (the cells without detectable Flag-Orf6) were quantified, and the ratios between the nuclear and the cytoplasmic signals (N/C ratio) of oligo dT staining (N/C ratio) were calculated (three biological replicates, $n > 21$ cells per replicate). The mean values of the N/C ratios for each biological replicate were plotted as black filled circles. The individual observations were also plotted as grey dots. The dotted line ($\log_2(N/C) = 0$) denotes the position of equal signal intensities in the nucleus and in the cytoplasm. Multiple comparisons were carried out using a one-way ANOVA followed by pairwise Tukey HSD posthoc tests. N. S., not significant.

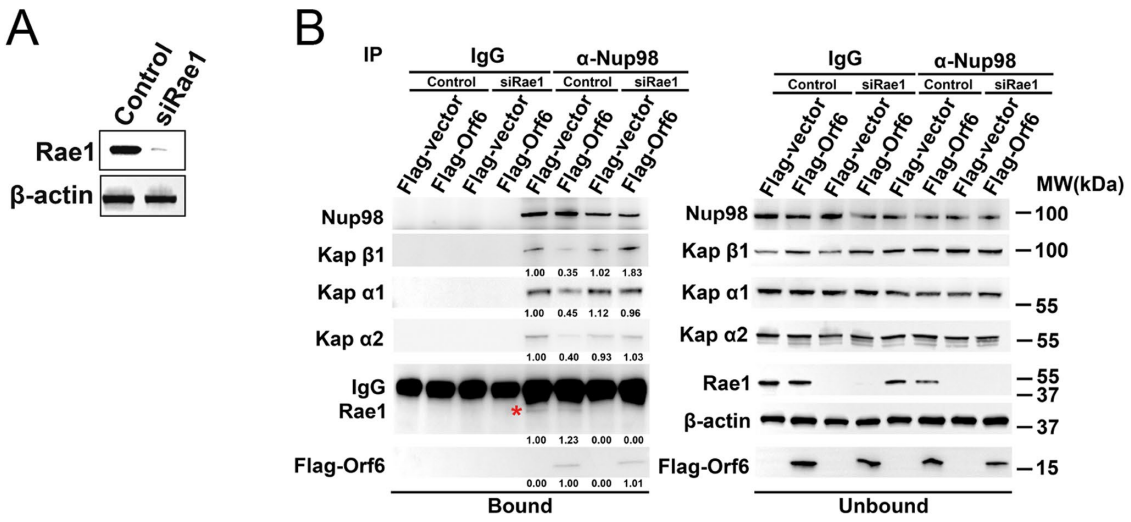


FIGURE 5: Rae1 is required for Orf6-mediated inhibition of Kap α and Kap β1 binding to Nup98. HEK293T cells were transfected with siRNA construct (control or siRae1) for 48 h, and then transfected with a plasmid encoding Flag-Orf6 (+) or vector control (-) for 24 h. Cell lysates were subjected to the immunoprecipitation experiment using anti-Nup98 antibodies. (A) Lysates of Rae1-depleted and control cells were analyzed by western blot using anti-Rae1 and anti-β-actin (loading control) antibodies. (B) Immunoprecipitation experiments were performed using the anti-Nup98 antibodies and nonspecific rabbit IgG coupled to beads. Bead bound (Bound) proteins and the flow-through (Unbound) fractions were analyzed by western blot using antibodies directed against the indicated proteins. A representative result of three biological replicates is shown. The abundances of proteins co-immunoprecipitated with beads were quantified, and the values were normalized with the control samples (for Kap α1, Kap α2, Kap β1, and Rae1 the control siRNA cells transfected with Flag-vector; for Flag-Orf6 the control siRNA transfected with Flag-Orf6). Red asterisk is adjacent to Rae1 band in control samples. The positions of molecular mass markers are shown.

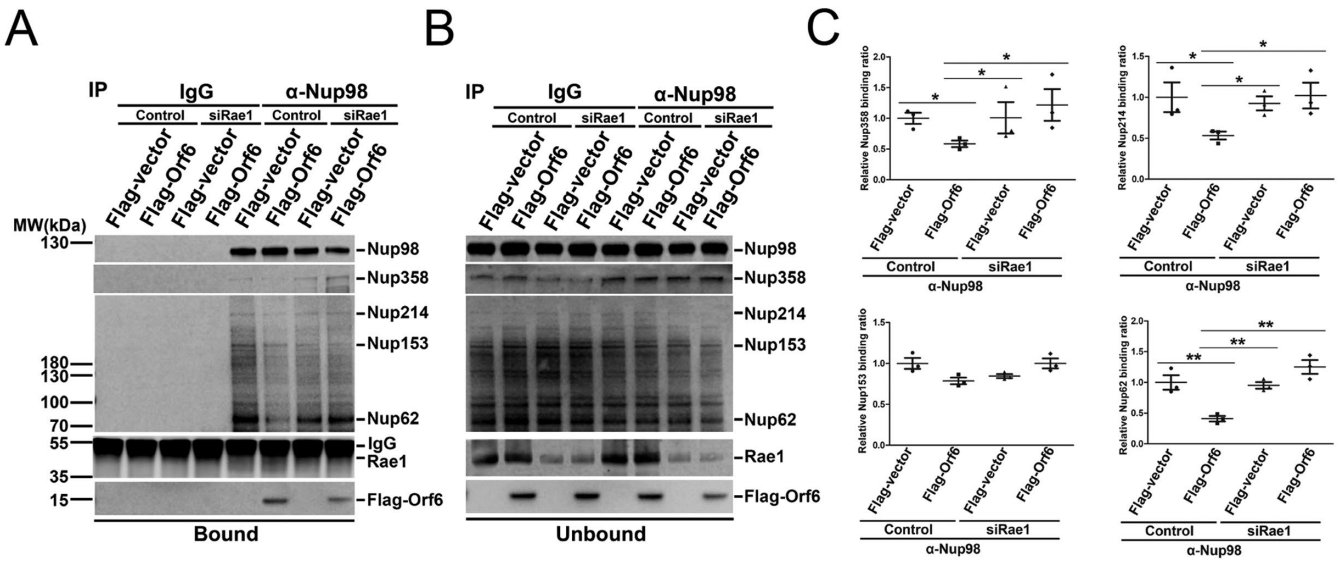


FIGURE 6: Orf6 reduces Nup98 binding to neighboring FG-Nups. (A and B) HEK293T cells were transfected with siRNA construct (control or siRae1) for 48 h, and then transfected with a plasmid encoding Flag-Orf6 (+) or vector control (–) for 24 h. Cell lysates were subjected to immunoprecipitation using anti-Nup98 antibodies and nonspecific rabbit IgG coupled to beads. Bead bound proteins (Bound, panel A) and proteins in the flow-through fractions (Unbound, panel B) were analyzed by western blot using antibodies directed against the indicated proteins. Note, mAb414 was used to detect Nup214, Nup153, and Nup62. A representative result of three biological replicates is shown. The positions of molecular mass markers are shown. (C) The abundances of proteins coimmunoprecipitated with beads, shown in (A), were quantified and normalized to bound Nup98. The ratio of values for Nup interactions with Nup98 in the presence and absence of Orf6 and containing WT or depleted levels of Rae1 are shown, with control (FLAG-vector, control siRNA) samples set to one. The individual observations of three biological replicates are shown in filled circles. The average values and the standard deviations are presented in the horizontal lines and the whiskers, respectively. *$p < 0.05$; **$p$,0.01.

strongly inhibited by Orf6 while activated HIF-1α and NF-κB p65 are only modestly affected (Xia *et al.*, 2020; Miyamoto *et al.*, 2022). NF-κB p65 can also be imported by the NTFs XPO7 and IPO8 (Liang *et al.*, 2013), and IPO4 and IPO7 are able to import HIF-1α (Chachami *et al.*, 2009), supporting the concept that not all pathways through the NPC are affected by Orf6.

Importantly, our observations that depletion of Rae1 suppresses the effects of Orf6 on p-STAT1 and mRNA transport seem to conflict with other suggested functions of Orf6 in these transport events, including the proposal that Orf6 blocks transport by directly binding p-STAT1 (Miyamoto *et al.*, 2022), by altering NTF localization, or by solely inhibiting the mRNA transport functions of Rae1 (Hall *et al.*, 2022; Li *et al.*, 2022). Furthermore, we find it difficult to envisage that Orf6 functions to merely physically clog the NPC (Addetia *et al.*, 2021). Considering the small size of the Orf6 (~7kD), the observed 1:1:1 stoichiometry of Orf6 bound to Nup98 and Rae1, and structural models suggesting Nup98 is present in 48 copies per NPC, the total mass of Orf6 per NPC would be relatively small (~340 kD) and distributed throughout the NPC. When one considers that expressing Nup98 tagged with GFP, which would position ~4 times the protein mass (i.e., GFP vs. Orf6) within a similar vicinity of the central channel (Rabut *et al.*, 2004), does not alter nuclear transport (Dultz *et al.*, 2008), it seems unlikely that Orf6 functions to physically obstruct the NPC.

Despite the clear effects of Orf6 on nuclear transport, it does not appear to play an essential role in SARS-CoV-2 virus replication. The sequence analysis of clinical isolates of the virus shows that Orf6 can occasionally be lost as a consequence of truncation or frameshift deletion of the viral genome, yet these viruses can still infect cells (Quéromès *et al.*, 2021). Furthermore, a recent study showed that a recombinant SARS-CoV-2 virus lacking the entire Orf6 coding region (Orf6Δ) replicates similar to WT virus in Vero cells and infects model animals (Kehrer *et al.*, 2023; Miyamoto *et al.*, 2022). These authors concluded that the main function of ORF6 during infection is to antagonize the antiviral innate immune response. Supporting this conclusion, genes involved in the pro-inflammatory response are more strongly upregulated in the cells infected with a Orf6Δ virus (Quéromès *et al.*, 2021) suggesting that in the absence of Orf6 unperturbed nucleocytoplasmic transport allows more robust proinflammatory signaling (NF-κB pathway; Miyamoto *et al.*, 2022). Our data showing SARS-CoV-2 virus production appears largely unaffected in Rae1-depleted cells (Figure 7; also see Gordon *et al.*, 2020a), where Orf6 is no longer functional in blocking nucleocytoplasmic transport (Figure 4), is consistent with those reported for the replication of Orf6Δ viruses.

The function of SARS-CoV-2 Orf6 in blocking nuclear transport also appears to influence the accumulation of specific viral proteins in the infected cells. Rae1 knock-down cells infected with SARS-CoV-2 showed visibly higher levels of specific viral proteins including spike, nucleocapsid, and Orf6 relative to control cells producing Rae1 (Figure 7, B and C). These results lead us to suggest that the Rae1-dependent functions of Orf6 include the regulation of specific viral protein production. Also consistent with this conclusion, a recent study showed cells infected with SARS-CoV-2 mutants lacking Orf6 contains elevated levels of the spike and nucleocapsid proteins (Kehrer *et al.*, 2023).

In summary, we propose that the interactions of Orf6 with the Rae1/Nup98 complex places Orf6 at a location within the NPC central channel where it disrupts specific FG-Nup interactions that function in protein import and mRNA export pathways. Through its ability to alter nuclear transport of distinct cargoes, Orf6 acts as an IFN antagonist, blocking both the import of p-STAT1 and IRF3 as well as the export of mRNAs encoding interferon stimulated genes (Hall *et al.*, 2022). Our results also show that the association of Orf6 with Rae1 also plays a role in regulating viral protein production in the infected cells. Whether this phenomena is directly related to the transport inhibitory function of Orf6 remains to be determined. Intriguingly, the interactions of Orf6 with Rae1 and Nup98 is not unique to this viral protein. Unrelated viruses also encode proteins, such as the M protein of VSV and herpesvirus Orf10, that bind to similar regions of Rae1 and Nup98 suggesting this NPC location represents a common evolutionary host target. In each case, these viral proteins have been proposed to inhibit nuclear export of mRNAs. Further understanding the impact of their association with Rae1 and Nup98 on NPC structure and transport may reveal strategies for suppressing their effects on the host immune response.

## MATERIALS AND METHODS

### Cell lines, viruses, and culture media

Vero E6 (ATCC), HEK293T (ATCC) cells are described (Kumar *et al.*, 2021). VIB cells, a Vero-related cell line, are gift from Dr. Michael Hendzel (Department of Oncology, University of Alberta). The genome of the VIB cell line lacks most type I interferon genes like Vero cells, but retains the interferon beta gene (IFNB1), and is permissive for SARS-CoV-2 infection (see Supplemental Figure S6A). SARS-CoV-2 (hCoV-19/Canada/ONVIDO-01/2020; GISAID accession no.: EPI_ISL_425177) was kindly provided by Darryl Falzarano (Vaccine and Infectious Disease Organization, Saskatoon, Canada). The infection experiment was carried out in the Biosafety level 3 facility in the Department of Medical Microbiology and Immunology, University of Alberta (Kumar *et al.*, 2021). Cells are cultured in Dulbecco's modified Eagles medium (DMEM; Life Technologies 11965-092) + 10% fetal bovine serum (FBS; Life Technologies 12483-020) + 1% Penicillin-Streptomycin solution (Life Technologies 15140-22) and placed in a humid incubator at 37°C with 5% $CO_2$. For inducing shRNA knock down, cells were treated with doxycycline (Sigma-Aldrich D9891) at a final concentration of 100 ng/mL. For IFN treatment experiments, cells were treated with IFN-α1 (Sigma-Aldrich SRP4596) at a final concentration of 10 U/μl.

### Transfection

The plasmid transfection was performed using Lipofectamine 3000 (Life Technologies) following the manufacturer's protocol. Per well of 24-well plates, 0.5 μg of pCI-neo-3xFlag-Orf6 (Miorin *et al.*, 2020), 1 μg P3000 and 1.5 μl Lipofectamine 3000 are mixed with optiMEM (Life Technologies 31985-070) to a final volume of 50 μl, and incubated for 20 min in room temperature. The mixture was added dropwise to the culture and incubated at 37°C for 6 h. Then, the wells were washed twice with phosphate-buffered saline (PBS), and incubated with the culture media at 37°C for the downstream experiment.

### Lentivirus production and transduction

The doxycycline-inducible short-hairpin RNA (Tet-shRNA) constructs for gene knock-down were introduced into the host genome using the lentivirus system (Naldini *et al.*, 1996). The lentiviral transfer plasmids harboring the Tet-shRNA constructs targeting Rae1 and Nup98/Nup96, and the scramble control (non-mammalian shRNA control), were produced by inserting the annealed oligonucleotides containing shRNA sequences (Supplemental Table S1) into Tet-pLKO-puro (Addgene #21915; Wiederschain *et al.*, 2009) at the AgeI/EcoRI restriction sites. The lentivirus pseudoparticles were produced in HEK293T cells as described (Li *et al.*, 2018). Briefly, HEK293T was transfected using Lipofectamine 3000 (Life Technologies) and a mixture of psPAX2 (Addgene #12260; gift from Didier

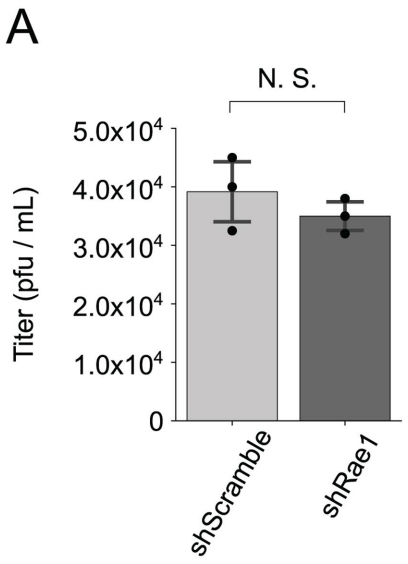
A
N. S.
Titer (pfu / mL)
5.0x10^4
4.0x10^4
3.0x10^4
2.0x10^4
1.0x10^4
0
shScramble
shRae1

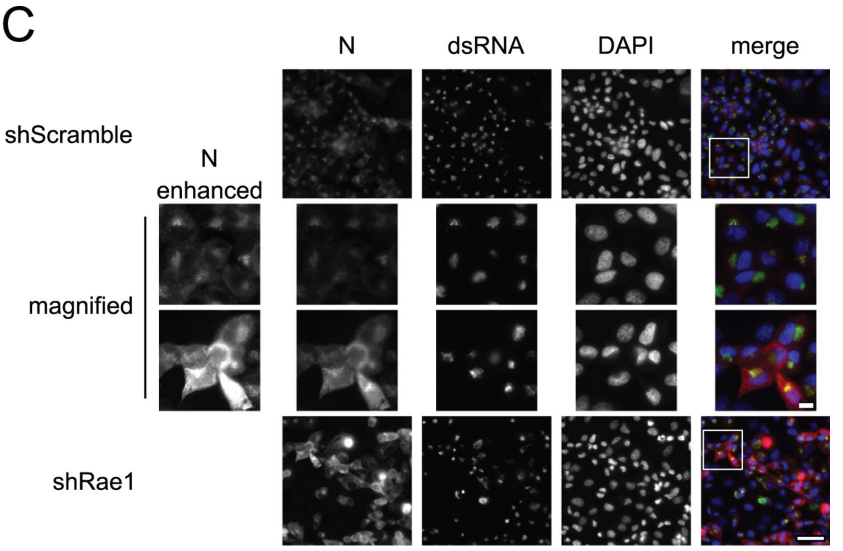
C
N
dsRNA
DAPI
merge
shScramble
N enhanced
magnified
shRae1

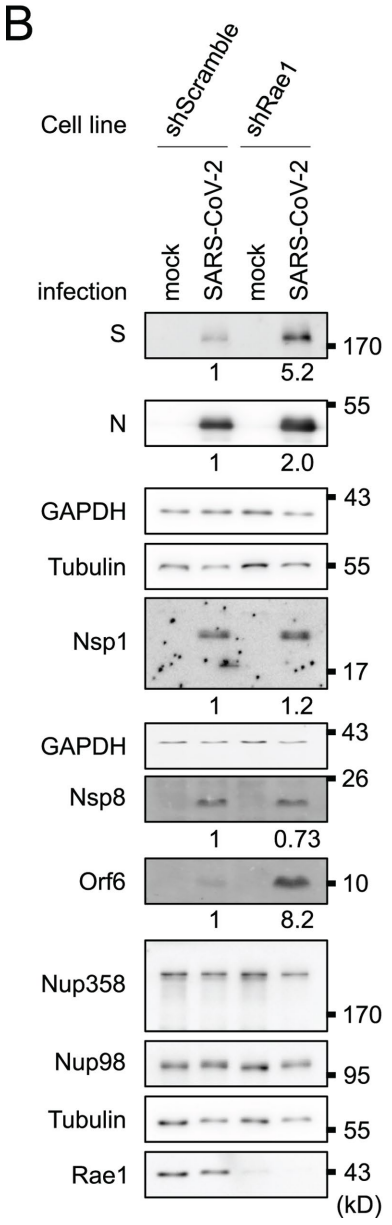
B
Cell line
shScramble
shRae1
infection
mock
SARS-CoV-2
mock
SARS-CoV-2
S
170
1
5.2
N
55
1
2.0
GAPDH
43
Tubulin
55
Nsp1
17
1
1.2
GAPDH
43
Nsp8
26
1
0.73
Orf6
10
1
8.2
Nup358
170
Nup98
95
Tubulin
55
Rae1
43
(kD)

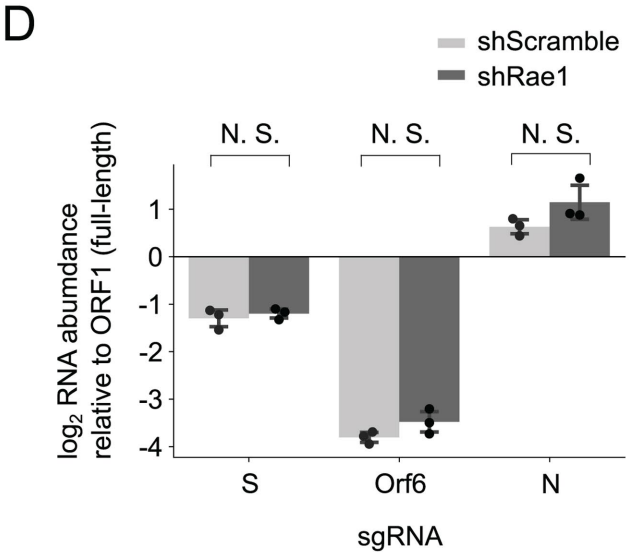
D
shScramble
shRae1
N. S.
N. S.
N. S.
log2 RNA abumdance relative to ORF1 (full-length)
1
0
-1
-2
-3
-4
S
Orf6
N
sgRNA

Trono), pMD2.G (Addgene #12259; gift from Didier Trono) and the lentivirus transfer plasmid containing the Tet-shRNA construct. The lentivirus pseudoparticles released to the culture supernatant were collected at 24 and 48 h posttransfection and then concentrated using Lenti-X concentrator (Clontech) following manufacturer's instructions. Lentivirus transduction for establishing cell lines harboring the Tet-shRNA constructs was performed using the reverse transduction methods. Detached Vero or VIB cells ($5 \times 10^4$ cells) in 100 µl DMEM + 8 µg/ml hexadimethrine bromide (Sigma-Aldrich) were seeded in a 24-well plate containing lentivirus suspension (0–10 µl) in 100 µl DMEM + 8 µg/ml hexadimethrine bromide. After 6 h of incubation at 37°C, 1 ml of culture media was added. At 48 h after the transduction, the cells were subjected to drug selection with 3 µg/ml puromycin. The selection media were changed every 2 d until the negative control samples (transduced without lentivirus) did not contain any viable cells. The drug-induced knock-down of the target genes was confirmed by western blot and immunofluorescence after the doxycycline treatment.

### Cell growth assay

The cells were seeded in sixwell plates. At time 0 h, the cells were subjected to a doxycycline treatment by replacing media with DMEM with or without 100 ng/mL doxycycline. At the indicated time after the drug treatment started, the cells were detached from the plates and the total cell numbers in the well were evaluated by manual counting using hemocytometer.

### Antibodies

Primary antibodies used in this study were: rabbit anti-Nup358 (Fontoura *et al.*, 2001), rabbit anti-Nup98 (Mitchell *et al.*, 2010), mouse anti-Rae1 (Santa Cruz sc-393252), mouse anti-α-Tubulin (Sigma-Aldrich T6074), rat anti-Nup96 (EMD Milipore MABE1039), mouse mAb414 (Abcam ab24609), mouse anti-FLAG (Sigma-Aldrich F1804), rabbit anti-phospho-STAT1(Tyr701; Cell Signaling #9167), rabbit anti-STAT1 (Cell Signaling #14994), mouse anti-Kap α2 (Abmart MK74864), mouse anti- Kap α1/importin α5 (Santa Cruz, sc-101292), mouse anti-Kap β1 (Abmart MG501718), mouse anti-β-actin (Sigma-Aldrich A5528), rabbit anti-Rae1 (ABclonal A6713), rabbit anti-Nup98 (ABclonal A0530), human anti-SARS-CoV-2 Spike, rabbit anti-SARS-CoV-2 NP (GeneTex GTX135357), rabbit anti-SARS-CoV-2 nsp1 (Zhang *et al.*, 2021), rabbit anti-GAPDH (Abcam ab133354), and rabbit anti-Kap α2 (Proteintech 10819-1-AP), mouse anti-Kap β1 (Abcam ab2811), sheep anti-SARS-CoV-2 Orf6 (MRC PPU Reagents and Services DA087), mouse anti-SARS-CoV-2 nsp8 (GeneTex GTX632696).

Secondary antibodies in this study were: HRP-conjugated goat anti-rabbit IgG (Bio-Rad 170-6515), HRP-conjugated goat anti-mouse IgG (Bio-Rad 170-6516), HRP-conjugated anti-rat IgG (Jackson ImmunoResearch 712-055-150), HRP-conjugated donkey anti-rabbit IgG and sheep anti-mouse IgG (GE Healthcare, NA934V and NA931V, respectively), HRP-conjugated anti-human IgG, Alexa488-conjugated donkey anti-rabbit IgG (Life Technologies A21206), Alexa488-conjugated donkey anti-mouse IgG (Life Technologies A21202), Alexa555-conjugated donkey anti-rabbit IgG (Life Technologies A31572), Alexa594-conjugated goat anti-rabbit IgG (Life Technologies A11012), Alexa594-conjugated donkey anti-mouse IgG (Life Technologies A21203), Alexa594-conjugated donkey anti-rat IgG (Jackson ImmunoResearch 712-585-153), and Alexa647-conjugated goat anti-rabbit IgG (Life Technologies A21246), Alexa647-conjugated donkey anti-sheep IgG (Jackson ImmunoResearch 713-605-003).

### Western blot

Cells were lysed in the lysis buffer (1% sodium dodecyl sulfate [SDS], 5% glycerol, 100 mM dithiothreitol [DTT], 100 mM Tris-HCl, pH 6.8) containing 1 mM phenylmethylsulfonyl fluoride [PMSF] and, if needed, 1:100 phosphatase inhibitor cocktail (Cell signaling). The samples were briefly sonicated (Branson Sonifer 250) and boiled at 65°C for 10 min. The samples were run on 8% SDS–PAGE gels and transferred onto nitrocellulose membranes (Bio-Rad). Membranes were blocked in PBS + 0.1% Tween 20 (PBS-T) containing 5% nonfat skim milk or 3% bovine serum albumin (BSA; when detecting phosphoproteins). The membranes were incubated with the primary antibodies (1:10,000 dilution, except for anti-Nup96 [1:1000]) in PBS-T + the blocking agents at 4°C overnight. After the washes (3 × 5 min) with PBS-T, the membranes were incubated with the secondary antibodies (either HRP- or Alexa647-conjugated; 1:10,000 dilution) in PBS-T + the blocking agents at room temperature for 1 h. The signals from the HRP-conjugated secondary antibodies were visualized using ECL (Cytiva) and recorded using ImageQuant LAS 4000 system (Cytiva). The signals from the Alexa647-conjugated secondary antibodies were imaged using Typhoon 9500 (Cytiva).

**FIGURE 7:** Rae1 depletion alters viral protein levels in SARS-CoV-2 infected cells. (A) VIB cells harboring a doxycycline-induced shRNA construct (shScramble or shRae1) were incubated in DMEM containing 100 ng/mL doxycycline for 48 h and then infected with SARS-CoV-2 for 24 h. Viral titers of culture supernatants where determined 24 h p.i.. Error bars indicate standard deviations. A Mann-Whitney U test was carried out to compare two samples. N. S.: not significant. (B) Rae1-depleted (shRae1) and control scramble knock-down cells (shScramble) were infected with SARS-CoV-2, or mock infected, as described in panel A. At 24 h p.i., cell lysates were analyzed by western blotting using antibodies directed against the indicated proteins. The relative protein abundances of the viral proteins between the SARS-CoV-2 infected Rae1 knock down cells and the corresponding scramble knock-down cells were quantified, and an average value of two biological replicates are presented underneath the blot images. The positions of molecular mass markers are also shown. (C) Infected Rae1-depleted (shRae1) and control scramble knock-down cells were also examined by IFM at 24 h p.i. using the anti-N (red in the merged images) and anti-dsRNA (green in the merged images) antibodies. The nuclei were counterstained with DAPI (blue in the merged images). The signal intensities of the images were adjusted using the same normalization parameters between the shScramble and shRae1 samples. Images reveal differences in N protein levels between infected Rae1-depleted cells and scramble control knock down cells. The magnified images of the regions indicated by white rectangles are shown in the middle two rows. Size bars in the full-scale images and magnified images are 50 and 10 µm. (D) Levels of the indicated subgenomic RNAs relative to the full-length genomic RNA were determined at 24 h p.i. in Rae1-depleted (shRae1) and control scramble knock down cells. Error bars indicate standard deviations. A Mann-Whitney U test was carried out to compare two samples ($N = 3$ biological replicates). N. S.: not significant.

### Immunofluorescence microscopy

The cells were seeded in 24-well plates containing 12-mm round coverslips (Fisher). The samples were fixed with 3.75% formaldehyde in PBS at room temperature for 10 min and washed twice with PBS. The cells were permeabilized with 0.5% Triton X-100 in PBS for 10 min, washed with PBS-T and blocked with PBS-T + 1% BSA at room temperature for 20 min. The samples were incubated with primary antibodies (1:1000 dilution, except for anti-Nup96 [1:100]) in PBS-T + 1% BSA at 4°C overnight. After washes (5 min x 3) with PBS-T + 0.1% BSA, the samples were incubated with the secondary antibodies (1:1000 dilution) in PBS-T + 1% BSA at room temperature for 1 h, then washed with PBS-T. The coverslips containing the cell samples were mounted on DAPI-fluoromountG (Southern Biotech).

### Fluorescence in-situ hybridization (FISH)

The FISH-IF experiment was performed essentially as described (Faria *et al.*, 2005). The cells were seeded in 24-well plates containing 12-mm round coverslips (Fisher). The samples were fixed with 3.75% formaldehyde in PBS at room temperature for 10 min and washed twice with PBS. The cells were permeabilized with PBS + 0.2% Triton X-100 at room temperature for 10 min, and incubated with the primary antibodies (1:1000 dilution) in PBS + 0.2% Triton X-100 + 2 mM VRC + 1 mM RNaseOUT (Invitrogen) for 30 min. After washes (5 min x 3) with PBS, the cells were fixed with 3.75% formaldehyde in PBS at room temperature for 10 min and then washed twice with PBS. The samples were further incubated with the prehybridization buffer (15% formamide in 1 × SSC) for 20 min. The hybridization was performed by incubation of the sample with hybridization buffer (15% formamide, 10% dextran sulfate, 0.2 µg/µl tRNA, 2 mM VRC, Texas Red-Oligo $dT_{50}$ in 1xSSC) at 37°C overnight. After washes (2 × 30 min) with the prehybridization buffer at 37°C, the cells were washed twice with PBS followed by incubation with the secondary antibodies (1:1000 dilution) in PBS at room temperature for 1 h, then washed with PBS (3 × 5 min). The coverslips containing the cell samples were mounted on DAPI-fluoromountG (Southern Biotech).

### Microscope observations and Image analysis

Series of z-stack images of the samples (IF and FISH) were acquired using DeltaVision Elite imaging system (Cytiva) equipped with a PlanApo N 60x/1.42 NA oil objective (Olympus) at 0.24 µm intervals along the z-axis. Images were deconvolved with the deconvolution module of the SoftWoRx software (Cytiva) under a "conservative" setting. Deconvolved images were further processed (crop and normalization for presentation) with ImageJ (NIH). The signal intensity quantification was performed on CellProfiler (Stirling *et al.*, 2021) and ImageJ. For each cell, a single slice containing the equatorial section of the nucleus was selected for the analysis. After the background correction, the integral signal intensities in the regions of the nucleus, the cytoplasm and the nuclear periphery (the regions within 2 pixels of the cytoplasmic and the nucleoplasmic sides of the nuclear boundary) were measured. The integral signal intensities in the regions of interest were divided by the area to yield the normalized signal intensities. The N/C ratios were calculated as the ratios between the normalized signal intensities in the nucleus and the cytoplasm. The spot counting of nucleoporins (Nup358 and Nup96) in the three-dimensional images of nuclei was performed on Imaris software (Oxford instruments).

### Immunoprecipitation

HEK293T cells were cultured in sixwell plates. Rae1 (and control) knockdown was initiated by transfection with a pool of four siRNA (50 nM each, L-011482-01-0005 (Dharmacon) for Rae1 knockdown, D-001810-10-05 (Dharmacon) for control knock-down) using Lipofectamine RNAimax (Invitrogen) for a total of 48 h. The cells were further transfected with 3 µg of 3xFlag vector or 3 µg of 3xFlag-Orf6 using Lipofectamine 3000 (Invitrogen) for the last 24 h. The immunoprecipitation was performed essentially as described (Zhang *et al.*, 2021). Total cell pellet was lysed in 50 mM Tris-HCl (pH 7.5), 150 mM NaCl, 1% IGEPAL-CA630, 1 mM DTT, 1 mM EDTA, 1 mM PMSF, 1x cOmplete protease inhibitor cocktail (Roche) and 10% glycerol for 30 min on ice and vortexed every 5 min, followed by sonicating. The lysates were cleared by a centrifugation at 13,000 *g* for 10 min. The supernatant was applied to 10 µl Protein A agarose beads (Invitrogen) conjugated with 2 µg rabbit anti-Nup98 antibodies (ABclonal) or 2 µg rabbit IgG (Sigma) overnight at 4°C. Beads were washed five times with lysis buffer at 4°C. Then, the proteins bound to the beads were eluted using SDS–PAGE sample buffer and subjected to SDS–PAGE, followed by western blot.

### RNA extraction and RT-qPCR

The total RNA was extracted using TRIzol (Life Technologies) following the manufacturer's protocol. One micro gram of total RNA was subjected to the reverse transcription using the Superscript II kit (Life Technologies). The relative gene abundance in the cDNA sample was examined by the quantitative PCR (qPCR) experiment on MX3000 (Agilent) using PerfeCTa SYBR green PCR mix (Quanta Bioscience). Oligonucleotides for the reaction were summarized in Supplemental Table S2. The pairs of primers (the forward primer in the leader sequence and the reverse primer in each ORF) were designed to amplify cDNAs of specific SARS-CoV-2 subgenomic RNAs (sgRNAs; Thorne *et al.*, 2022). The sgRNA level were evaluated by the $\Delta\Delta C_T$ method (Livak and Schmittgen, 2001). The $C_T$ value for each RNA target was normalized against the internal control (*ACTB*) to give the $\Delta C_T$ value. The $\Delta\Delta C_T$ was calculated as a difference in $\Delta C_T$ values between the sgRNAs and the full-length RNA of SARS-CoV-2. The sgRNA levels was given as $2^{-\Delta\Delta CT}$, based on the assumption that amplification efficiency of the PCR reaction is 100%.

### Statistics

Quantified data were subjected to a statistical analysis using either Microsoft Excel or a Python script using a package Pingouin (Vallat, 2018). The statistical analysis was performed after the observations within a biological replicate were summarized (mean values). The data were tested with a one-way ANOVA followed by pairwise Tukey HSD tests (for multiple comparisons), or a Student's *t* test or a Mann-Whitney U test (comparing two groups). The test results were indicated as following notations. N. S.: not significant ($p >= 0.05$), *: $p < 0.05$, **: $p < 0.01$, ***: $p < 0.001$.


## ACKNOWLEDGMENTS

We thank members of the Aitchison, Fontoura, and Wozniak labs for helpful discussions. We also thank Ray Ishida for assistance with the SARS-CoV-2 infections experiments. Funding for this work is supported by the Canadian Institutes of Health Research (FRN: 156030) to R.W.W., the National Institutes of Health, USA (NCDIR: 2P41GM109824-06 and R01 2R01GM112108-05 to J.D.A. and U54CA260560 and U19AI171443 to B.M.A.F.), the Career Enhancement Program Award (SPORE P50 CA070907 to B.M.A.F.), National Natural Science Foundation of China (82341052) to K.Z., and the Li Ka Shing Institute of Virology at the Univ. of Alberta (stipend support for N.L.).

## REFERENCES


Addetia A, Lieberman NAP, Phung Q, Hsiang T-Y, Xie H, Roychoudhury P, Shrestha L, Loprieno MA, Huang M-L, Gale M, *et al*. (2021). SARS-CoV-2 ORF6 disrupts bidirectional nucleocytoplasmic transport through interactions with Rae1 and Nup98. mBio 12, e00065-21.

Babu JR, Jeganathan KB, Baker DJ, Wu X, Kang-Decker N, Van Deursen JM (2003). Rae1 is an essential mitotic checkpoint regulator that cooperates with Bub3 to prevent chromosome missegregation. J Cell Biol 160, 341–353.

Bachi A, Braun IC, Rodrigues JP, Panté N, Ribbeck K, Von Kobbe C, Kutay U, Wilm M, Görlich D, Carmo-Fonseca M, Izaurralde E (2000). The C-terminal domain of TAP interacts with the nuclear pore complex and promotes export of specific CTE-bearing RNA substrates. RNA 6, 136–158.

Barbato S, Kapinos LE, Rencurel C, Lim RYH (2020). Karyopherin enrichment at the nuclear pore complex attenuates Ran permeability. J Cell Sci 133, jcs238121.

Blevins MB, Smith AM, Phillips EM, Powers MA (2003). Complex formation among the RNA export proteins Nup98, Rae1/Gle2, and TAP. J Biol Chem 278, 20979–20988.

Bley CJ, Nie S, Mobbs GW, Petrovic S, Gres AT, Liu X, Mukherjee S, Harvey S, Huber FM, Lin DH, *et al*. (2022). Architecture of the cytoplasmic face of the nuclear pore. Science 376, eabm9129.

Castelló A, Izquierdo JM, Welnowska E, Carrasco L (2009). RNA nuclear export is blocked by poliovirus 2A protease and is concomitant with nucleoporin cleavage. J Cell Sci 122, 3799–3809.

Chachami G, Paraskeva E, Mingot JM, Braliou GG, Görlich D, Simos G (2009). Transport of hypoxia-inducible factor HIF-1α into the nucleus involves importins 4 and 7. Biochem Biophys Res Commun 390, 235–240.

Dultz E, Zanin E, Wurzenberger C, Braun M, Rabut G, Sironi L, Ellenberg J (2008). Systematic kinetic analysis of mitotic dis- and reassembly of the nuclear pore in living cells. J Cell Biol 180, 857–865.

Faria PA, Chakraborty P, Levay A, Barber GN, Ezelle HJ, Enninga J, Arana C, van Deursen J, Fontoura BMA (2005). VSV disrupts the Rae1/mrnp41 mRNA nuclear export pathway. Mol Cell 17, 93–102.

Finlay DR, Newmeyer DD, Price TM, Forbes DJ (1987). Inhibition of in vitro nuclear transport by a lectin that binds to nuclear pores. J Cell Biol 104, 189–200.

Fischer J, Teimer R, Amlacher S, Kunze R, Hurt E (2015). Linker Nups connect the nuclear pore complex inner ring with the outer ring and transport channel. Nat Struct Mol Biol 22, 774–781.

Fontoura BMA, Blobel G, Matunis MJ (1999). A conserved biogenesis pathway for nucleoporins: Proteolytic processing of a 186-kilodalton precursor generates Nup98 and the novel nucleoporin, Nup96. J Cell Biol 144, 1097–1112.

Fontoura BMA, Dales S, Blobel G, Zhong H (2001). The nucleoporin Nup98 associates with the intranuclear filamentous protein network of TPR. Proc Natl Acad Sci 98, 3208–3213.

Frieman M, Yount B, Heise M, Kopecky-Bromberg SA, Palese P, Baric RS (2007). Severe acute respiratory syndrome coronavirus ORF6 antagonizes stat1 function by sequestering nuclear import factors on the rough endoplasmic reticulum/golgi membrane. J Virol 81, 9812–9824.

Gao X, Tian H, Zhu K, Li Q, Hao W, Wang L, Qin B, Deng H, Cui S (2022). Structural basis for Sarbecovirus ORF6 mediated blockage of nucleocytoplasmic transport. Nat Commun 13, 1–11.

Gong D, Kim YH, Xiao Y, Du Y, Xie Y, Lee KK, Feng J, Farhat N, Zhao D, Shu S, *et al*. (2016). A herpesvirus protein selectively inhibits cellular mRNA nuclear export. Cell Host and Microbe 20, 642–653.

Gordon DE, Hiatt J, Bouhaddou M, Rezelj V, Ulferts S, Braberg H, Jureka AS, Obernier K, Guo JZ, Batra J, *et al*. (2020a). Comparative host-coronavirus protein interaction networks reveal pan-viral disease mechanisms. Science 370, eabe9403.

Gordon DE, Jang GM, Bouhaddou M, Xu J, Obernier K, White KM, O'Meara MJ, Rezelj VV, Guo JZ, Swaney DL, *et al*. (2020b). A SARS-CoV-2 protein interaction map reveals targets for drug repurposing. Nature 583, 459–468.

Gustin KE, Sarnow P (2001). Effects of poliovirus infection on nucleo-cytoplasmic trafficking and nuclear pore complex composition. EMBO J 20, 240–249.

Hall R, Guedán A, Yap MW, Young GR, Harvey R, Stoye JP, Bishop KN (2022). SARS-CoV-2 ORF6 disrupts innate immune signalling by inhibiting cellular mRNA export. PLoS Pathog 18, e1010349.

Hanover JA, Cohen CK, Willingham MC, Park MK (1987). O-linked N-acetylglucosamine is attached to proteins of the nuclear pore. Evidence for cytoplasmic and nucleoplasmic glycoproteins. J Biol Chem 262, 9887–9894.

Hayama R, Rout MP, Fernandez-Martinez J (2017). The nuclear pore complex core scaffold and permeability barrier: variations of a common theme. Curr Opin Cell Biol 46, 110–118.

Hoffmann HH, Schneider WM, Rice CM (2015). Interferons and viruses: an evolutionary arms race of molecular interactions. Trends Immunol 36, 124–138.

Holt GD, Snow CM, Senior A, Haltiwanger RS, Gerace L, Hart GW (1987). Nuclear pore complex glycoproteins contain cytoplasmically disposed O-linked N-acetylglucosamine. J Cell Biol 104, 1157–1164.

Hoogenboom BW, Hough LE, Lemke EA, Lim RYH, Onck PR, Zilman A (2021). Physics of the nuclear pore complex: Theory, modeling, and experiment. Phys Rep 921, 1–53.

Ivashkiv LB, Donlin LT (2014). Regulation of type I interferon responses. Nature Reviews. Immunology 14, 36–49.

Kehrer T, Cupic A, Ye C, Yildiz S, Bouhhadou M, Crossland NA, Barrall E, Cohen P, Tseng A, Çağatay T, *et al*. (2023). Impact of SARS-CoV-2 ORF6 and its variant polymorphisms on host responses and viral pathogenesis. Cell Host Microbe 31, 1668–1684.

Kraemer D, Blobel G (1997). mRNA binding protein mrnp 41 localizes to both nucleus and cytoplasm. Proc Nat Acad Sci USA 94, 9119–9124.

Kumar A, Ishida R, Strilets T, Cole J, Lopez-Orozco J, Fayad N, Felix-Lopez A, Elaish M, Evseev D, Magor KE, *et al*. (2021). SARS-CoV-2 nonstructural Protein 1 inhibits the interferon response by causing depletion of key host signaling factors. J Virol 95, e0026621.

Li Y, Bakke J, Finkelstein D, Zeng H, Wu J, Chen T (2018). HNRNPH1 is required for rhabdomyosarcoma cell growth and survival. Oncogenesis 7, 1–13.

Li T, Wen Y, Guo H, Yang T, Yang H, Ji X (2022). Molecular mechanism of SARS-CoVs Orf6 targeting the Rae1–Nup98 complex to compete with mRNA nuclear export. Front Mol Biosci 8, 813248.

Liang P, Zhang H, Wang G, Li S, Cong S, Luo Y, Zhang B (2013). KPNB1, XPO7 and IPO8 mediate the translocation ofNF-κB/p65 into the nucleus. Traffic 14, 1132–1143.

Lim RYH, Huang B, Kapinos LE (2015). How to operate a nuclear pore complex by Kap-centric control. Nucleus 6, 366–372.

Livak KJ, Schmittgen TD (2001). Analysis of relative gene expression data using real-time quantitative PCR and the 2(-Delta C(T)) Method. Methods (San Diego. Calif.) 25, 402–408.

Marelli M, Aitchison JD, Wozniak RW (1998). Specific binding of the karyopherin Kap121p to a subunit of the nuclear pore complex containing Nup53p, Nup59p, and Nup170p. J Cell Biol 143, 1813–1830.

McBride KM, Banninger G, McDonald C, Reich NC (2002). Regulated nuclear import of the STAT1 transcription factor by direct binding of importin-α. EMBO J 21, 1754–1763.

Miorin L, Kehrer T, Sanchez-Aparicio MT, Zhang K, Cohen P, Patel RS, Cupic A, Makio T, Mei M, Moreno E, *et al*. (2020). SARS-CoV-2 Orf6 hijacks Nup98 to block STAT nuclear import and antagonize interferon signaling. Proc Nat Acad Sci USA 117, 28344–28354.

Mitchell JM, Mansfeld J, Capitanio J, Kutay U, Wozniak RW (2010). Pom121 links two essential subcomplexes of the nuclear pore complex core to the membrane. J Cell Biol 191, 505–521. https://doi.org/10.1083/jcb.201007098

Miyamoto Y, Itoh Y, Suzuki T, Tanaka T, Sakai Y, Koido M, Hata C, Wang C-X, Otani M, Moriishi K, *et al*. (2022). SARS-CoV-2 ORF6 disrupts nucleocytoplasmic trafficking to advance viral replication. Commun Biol 5, 483.

Mohr D, Frey S, Fischer T, Güttler T, Görlich D (2009). Characterization of the passive permeability barrier of nuclear pore complexes. EMBO J 28, 2541–2553.

Mosalaganti S, Obarska-Kosinska A, Siggel M, Taniguchi R, Turoňová B, Zimmerli CE, Buczak K, Schmidt FH, Margiotta E, Mackmull MT, *et al*. (2022). AI-based structure prediction empowers integrative structural analysis of human nuclear pores. Science 376, eabm9506.

Naldini L, Blömer U, Gallay P, Ory D, Mulligan R, Gage FH, Verma IM, Trono D (1996). In vivo gene delivery and stable transduction of nondividing cells by a lentiviral vector. Science 272(April), 263–267.

Newmeyer DD, Forbes DJ (1988). Nuclear import can be separated into distinct steps in vitro: Nuclear pore binding and translocation. Cell 52, 641–653.

Powers MA, Forbes DJ, Dahlberg JE, Lund E (1997). The vertebrate GLFG nucleoporin, Nup98, is an essential component of multiple RNA export pathways. J Cell Biol 136, 241–250.

Pritchard CEJ, Fornerod M, Kasper LH, Van Deursen JMA (2000). RAE1 is a shuttling mRNA export factor that binds to a GLEBS-like NUP98 motif at the nuclear pore complex through multiple domains. J Cell Biol 145, 237–253.

Quan B, Seo HS, Blobel G, Ren Y (2014). Vesiculoviral matrix (M) protein occupies nucleic acid binding site at nucleoporin pair (Rae1•Nup98). Proc Nat Acad Sci USA 111, 9127–9132.

Quéromès G, Destras G, Bal A, Regue H, Burfin G, Brun S, Fanget R, Morfin F, Valette M, Trouillet-Assant S, *et al*. (2021). Characterization of SARS-CoV-2 ORF6 deletion variants detected in a nosocomial cluster during routine genomic surveillance, Lyon, France. Emerging Microbes and Infections 10, 167–177.

Rabut G, Doye V, Ellenberg J (2004). Mapping the dynamic organization of the nuclear pore complex inside single living cells. Nat Cell Biology 6, 1114–1121.

Raftery N, Stevenson NJ (2017). Advances in anti-viral immune defense: revealing the importance of the IFN JAK/STAT pathway. Cell Mol Life Sci 74, 2525–2535.

Rajani KR, Pettit Kneller EL, McKenzie MO, Horita DA, Chou JW, Lyles DS (2012). Complexes of Vesicular Stomatitis Virus Matrix Protein with Host Rae1 and Nup98 Involved in Inhibition of Host Transcription. PLoS Pathog 8, e1002929.

Satterly N, Tsai P-L, van Deursen J, Nussenzveig DR, Wang Y, Faria PA, Levay A, Levy DE, Fontoura BMA (2007). Influenza virus targets the mRNA export machinery and the nuclear pore complex. Proc Nat Acad Sci USA 104, 1853–1858.

Schoggins JW (2019). Interferon-Stimulated Genes: What Do They All Do? Annual Review of Virology 6, 567–584.

Sekimoto T, Imamoto N, Nakajima K, Hirano T, Yoneda Y (1997). Extracellular signal-dependent nuclear import of Stat1 is mediated by nuclear pore-targeting complex formation with NPI-1, but not Rch1. EMBO J 16, 7067–7077.

Shen Q, Wang YE, Palazzo AF (2021). Crosstalk between nucleocytoplasmic trafficking and the innate immune response to viral infection. J Biol Chem 297, 100856.

Sitterlin D (2004). Characterization of the Drosophila Rae1 protein as a G1 phase regulator of the cell cycle. Gene 326, 107–116.

Stirling DR, Swain-Bowden MJ, Lucas AM, Carpenter AE, Cimini BA, Goodman A (2021). CellProfiler 4: improvements in speed, utility and usability. BMC Bioinf 22, 1–11.

Strawn LA, Shen T, Shulga N, Goldfarb DS, Wente SR (2004). Minimal nuclear pore complexes define FG repeat domains essential for transport. Nat Cell Biology 6, 197–206.

Thorne LG, Bouhaddou M, Reuschl AK, Zuliani-Alvarez L, Polacco B, Pelin A, Batra J, Whelan MVX, Hosmillo M, Fossati A, *et al*. (2022). Evolution of enhanced innate immune evasion by SARS-CoV-2. Nature 602, 487–495.

Vallat R (2018). Pingouin: statistics in Python. J Open Source Software 3, 1026.

von Kobbe C, van Deursen JMA, Rodrigues JP, Sitterlin D, Bachi A, Wu X, Wilm M, Carmo-Fonseca M, Izaurralde E (2000). Vesicular stomatitis virus matrix protein inhibits host cell gene expression by targeting the nucleoporin Nup98. Mol Cell 6, 1243–1252.

Walther TC, Alves A, Pickersgill H, Loïodice I, Hetzer M, Galy V, Hülsmann BB, Köcher T, Wilm M, Allen T, *et al*. (2003). The conserved Nup107-160 complex is critical for nuclear pore complex assembly. Cell 113, 195–206.

Wiederschain D, Wee S, Chen L, Loo A, Yang G, Huang A, Chen Y, Caponigro G, Yao YM, Lengauer C, *et al*. (2009). Single-vector inducible lentiviral RNAi system for oncology target validation. Cell Cycle 8, 498–504.

Wu X, Kasper LH, Mantcheva RT, Mantchev GT, Springett MJ, van Deursen JM (2001). Disruption of the FG nucleoporin NUP98 causes selective changes in nuclear pore complex stoichiometry and function. Proc Nat Acad Sci USA 98, 3191–3196.

Xia H, Cao Z, Xie X, Zhang X, Chen JYC, Wang H, Menachery VD, Rajsbaum R, Shi PY (2020). Evasion of Type I Interferon by SARS-CoV-2. Cell Rep 33, 108234.

Xu W, Edwards MR, Borek DM, Feagins AR, Mittal A, Alinger JB, Berry KN, Yen B, Hamilton J, Brett TJ, *et al*. (2014). Ebola virus VP24 targets a unique NLS binding site on karyopherin alpha 5 to selectively compete with nuclear import of phosphorylated STAT1. Cell Host and Microbe 16, 187–200.

Zhang K, Shang G, Padavannil A, Wang J, Sakthivel R, Chen X, Kim M, Thompson MG, García-Sastre A, Lynch KW, *et al*. (2018). Structural–functional interactions of NS1-BP protein with the splicing and mRNA export machineries for viral and host gene expression. Proc Nat Acad Sci USA 115, E12218–E12227.

Zhang K, Xie Y, Muñoz-Moreno R, Wang J, Zhang L, Esparza M, García-Sastre A, Fontoura BMA, Ren Y (2019). Structural basis for influenza virus NS1 protein block of mRNA nuclear export. Nat Microbiol 4, 1671–1679.

Zhang K, Miorin L, Makio T, Dehghan I, Gao S, Xie Y, Zhong H, Esparza M, Kehrer T, Kumar A, *et al*. (2021). Nsp1 protein of SARS-CoV-2 disrupts the mRNA export machinery to inhibit host gene expression. Sci Adv 7, 1–13.